remote sensing

MDPI

Review

Multi-Sensor Precipitation Estimation from Space: Data Sources, Methods and Validation

Ruifang Guo [1], Xingwang Fan [2,3], Han Zhou [4] and Yuanbo Liu [2,3,*]

[1] College of Geography Science, Inner Mongolia Normal University, Hohhot 010022, China; rfguo@imnu.edu.cn
[2] Key Laboratory of Lake and Watershed Science for Water Security, Nanjing Institute of Geography and Limnology, Chinese Academy of Sciences, Nanjing 21135, China; xwfan@niglas.ac.cn
[3] Key Laboratory of Watershed Geographic Sciences, Nanjing Institute of Geography and Limnology, Chinese Academy of Sciences, Nanjing 21135, China
[4] School of Resource and Environmental Engineering, Wuhan University of Technology, Wuhan 430070, China; hanzhou0925@whut.edu.cn
* Correspondence: ybliu@niglas.ac.cn

Abstract: Satellite remote sensing complements rain gauges and ground radars as the primary sources of precipitation data. While significant advancements have been made in spaceborne precipitation estimation since the 1960s, the emergence of multi-sensor precipitation estimation (MPE) in the early 1990s revolutionized global precipitation data generation by integrating infrared and microwave observations. Among others, Global Precipitation Measurement (GPM) plays a crucial role in providing invaluable data sources for MPE by utilizing passive microwave sensors and geostationary infrared sensors. MPE represents the current state-of-the-art approach for generating high-quality, high-resolution global satellite precipitation products (SPPs), employing various methods such as cloud motion analysis, probability matching, adjustment ratios, regression techniques, neural networks, and weighted averaging. International collaborations, such as the International Precipitation Working Group and the Precipitation Virtual Constellation, have significantly contributed to enhancing our understanding of the uncertainties associated with MPEs and their corresponding SPPs. It has been observed that SPPs exhibit higher reliability over tropical oceans compared to mid- and high-latitudes, particularly during cold seasons or in regions with complex terrains. To further advance MPE research, future efforts should focus on improving accuracy for extremely low- and high-precipitation events, solid precipitation measurements, as well as orographic precipitation estimation.

Keywords: multi-sensor precipitation estimation; satellite precipitation product; validation; global precipitation measurement

check for updates

Citation: Guo, R.; Fan, X.; Zhou, H.; Liu, Y. Multi-Sensor Precipitation Estimation from Space: Data Sources, Methods and Validation. *Remote Sens.* **2024**, *16*, 4753. https://doi.org/10.3390/rs16244753

Academic Editors: Haonan Chen and Haoran Li

Received: 18 September 2024
Revised: 12 December 2024
Accepted: 17 December 2024
Published: 20 December 2024

Copyright: © 2024 by the authors. Licensee MDPI, Basel, Switzerland. This article is an open access article distributed under the terms and conditions of the Creative Commons Attribution (CC BY) license (https://creativecommons.org/licenses/by/4.0/).

1. Introduction

Precipitation is a crucial component of the hydrological cycle [1,2] and plays a pivotal role in maintaining the energy balance [3]. Accurately quantifying precipitation poses a significant challenge due to its non-normal distribution and substantial spatiotemporal variabilities [4–7]. Typically, precipitation can be observed through rain gauges or retrieved using ground-based radars and satellite sensors (Figure 1). Station measurements of precipitation have been recorded since the late 1890s. The distribution of these stations around the globe is uneven, with a tendency for sparser coverage of high-elevation regions and oceans. Moreover, inconsistencies arise in station measurements due to instrument replacements and variations in data preprocessing [8,9]. The availability of precipitation-measuring ground radar dates back to the 1950s [10], and these instruments have been utilized as alternative means for obtaining accurate precipitation data since the 1970s [10,11]. However, the limited coverage of such instruments around the globe is primarily attributed to their exorbitant operational and maintenance costs. Furthermore, radar data suffer from unavailability or are compromised due to range effects and beam blockage [12–14]. In contrast to ground-based observations, satellites

offer a "top-down" approach for estimating precipitation with unparalleled spatiotemporal coverage and the ability to bridge data gaps in remote and unsampled regions [15,16].

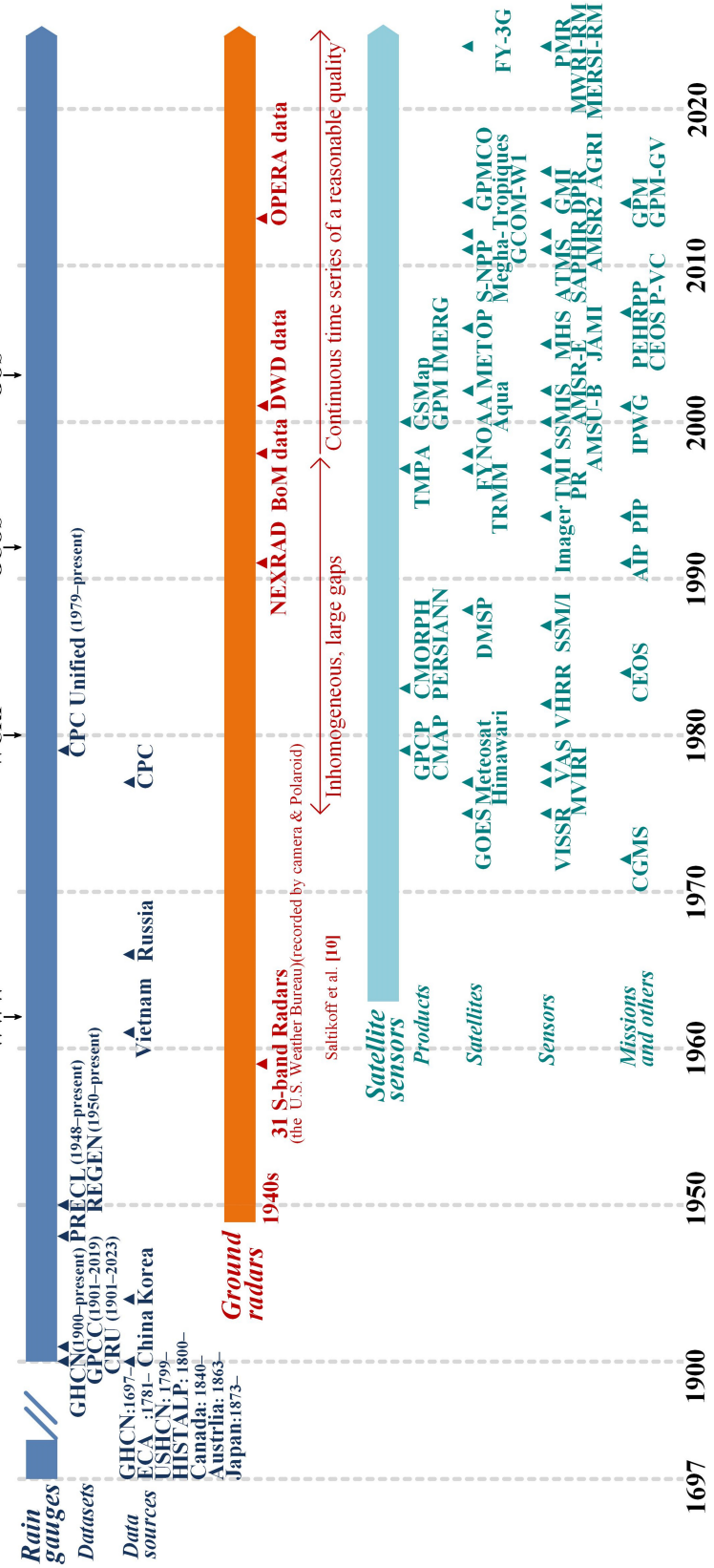

Figure 1. A brief history of precipitation-observing techniques, experiments, and products.

Satellite data have been utilized for precipitation estimation for over six decades, with satellite precipitation estimation (SPE) primarily relying on brightness temperature (TB) obtained from low-Earth orbit (LEO) and geostationary (GEO) infrared (IR) sensors as well as passive microwave (PMW) sensors. Although IR data possess high spatiotemporal resolution, the relationship between cloud-top temperature and precipitation is indirect [17]. PMW data offer a direct inference of precipitation compared to IR data [18]. However, the former are currently accessible from LEO satellites with a spatial resolution typically below 5×5 km. Launched in 1997, the Tropical Rainfall Measurement Mission (TRMM) carried a precipitation radar (PR) [19] that remained operational until April 2015. The launch of the TRMM marked a significant milestone in the advancement of precipitation retrieval using active microwave (AMW) sensors. Subsequently, in 2014, the Global Precipitation Measurement (GPM) Core Satellite was deployed with a dual-frequency radar (DPR), greatly enhancing the development of SPE [20,21]. Despite being the most accurate, PRs and DPRs are currently employed as calibration references for obtaining global precipitation data. For instance, they provide vertical hydrometeor profiles utilized by the Goddard Profiling Algorithm (GPROF) to establish the foundation for PMW-based rain rate retrievals.

IR, PMW, and AMW each possess distinct advantages and disadvantages. As a result, in the early 1990s, multi-sensor precipitation estimation (MPE) emerged with the objective of harnessing the benefits of multi-sensor methods while mitigating their limitations [22,23]. MPE was defined by Turk et al. [24] as a methodology that integrates IR- with PMW-based precipitation estimates through mathematical manipulations, resulting in a refined final product. Since its initial success, MPE has emerged as a widely accepted method for SPE, particularly since the 2000s. MPE has emerged as a prevalent approach for acquiring high-resolution and high-accuracy global satellite precipitation products (SPPs). Presently, the primary SPPs encompass TRMM Multi-Satellite Precipitation (TMPA) [25], Climate Prediction Center (CPC) morphing (CMORPH) [26], Global Satellite Mapping of Precipitation (GSMaP) [27], Precipitation Estimation from Remotely Sensed Information using Artificial Neural Network (PERSIANN) [28,29], and the Integrated Multi-satellite Retrievals for GPM (IMERG) [30].

Numerous reviews on SPE have been published from diverse perspectives, as shown in Table 1. These reviews have predominantly focused on the visible/infrared (VIS/IR)-based or PMW-based approaches during the 1990s, with an increased emphasis on global coverage after the 2000s. Several reviews have focused on global SPPs from the aspects of algorithms, datasets, validation, and applications. Others have addressed SPP applications and programs. Additionally, several books related to SPE have been published. Despite extensive efforts, there has been a limited number of reviews specifically addressing MPE. Given that MPE serves as the primary approach for obtaining global SPPs, it is imperative to provide a comprehensive review of its data sources, physical foundations, methodologies, and uncertainties. Such a review will (1) stimulate the development of novel MPE approaches, (2) facilitate the expansion of global precipitation data in terms of both temporal coverage and spatial resolution, and (3) enhance our understanding of MPE. The review is organized as follows: Section 2 introduces the satellites and sensors employed for precipitation estimation, followed by a comprehensive discussion of the underlying physical principles in Section 3. Section 4 provides an overview of the primary methodologies utilized for MPE. The subsequent section, Section 5, elucidates the development of SPPs and is succeeded by a thorough validation in Section 6. Finally, Section 7 concludes this discourse on MPE while proposing future prospects.

Table 1. Summary of existing review papers on SPE.

Theme	References
VIS/IR	[31]
PMW	[18,32,33]
VIS/IR, PMW	[8,34–37]

Table 1. *Cont.*

Theme	References
VIS/IR, PMW, AMW, MPE	[38–51]
Products	[52–54]
Validation	[55–58]
Applications	[15,59]
Programs/Projects	[60–65]
Books	[66–68]

2. Satellites and Sensors

Since the 1960s, satellite observations have been utilized to obtain atmospheric parameters. The World Weather Watch (WWW) program, initiated by the World Meteorological Organization (WMO) in 1963, effectively coordinates surface and satellite observational capabilities through the Global Observing System (GOS), encompassing a network of GEO and polar-orbiting satellites. The satellites are utilized for observing, recording, and reporting information pertaining to weather, climate, and the natural environment in order to facilitate forecasting and warning services. Subsequent to the initiation of this program, there has been a notable increase in the number of launched satellites. Consequently, these platforms along with their onboard payloads have emerged as the primary sources of data for global precipitation estimation.

MPEs primarily utilize high-resolution GEO IR images and highly precipitation-sensitive LEO PMW images (Table 2). The provision of GEO satellite data dates back to late 1974 when the National Aeronautics and Space Administration (NASA) launched the Synchronous Meteorological Satellites-1. With more satellites in the 1970s, daily global coverage GEO data became available, except for in polar regions [52]. Typically, IR images have a spatial resolution of between 1 and 4 km and a temporal resolution of between 10 and 30 min. The high spatiotemporal resolution facilitates the detection of cloud evolution and motion, thereby enhancing algorithm development (e.g., [69,70]). The provision of temporally continuous PMW data dates back to 1987 with the Defense Meteorological Satellite Program (DMSP). Numerous algorithms have been developed since then as more satellites have been launched [71,72]. Note that most PMW instruments have a spatial resolution of less than 5 km, particularly at lower frequencies.

Table 2. Major sensors used for precipitation estimation (see Addendum 1 for abbreviation details). For GEO satellites (Geostationary Operational Environmental Satellite (GOES), Meteosat, Himawari, FY, and INSAT series), the temporal resolution refers to the time taken by the satellite to scan the entire disk. For LEO satellites (DMSP, NOAA, Suomi National Polar-orbiting Partnership (S-NPP), TRMM, GPM Core Observatory (GPMCO), Global Change Observation Mission for Water (GCOM-W1), Meteorological operational satellite (METOP), Aqua and Megha-Tropiques), the nominal temporal resolution is 12 h (with two overpasses per satellite per day), although there may be gaps between swaths, resulting in some locations receiving only one overpass from each satellite per day. Additionally, the footprint size of PMW imagery varies with frequency; therefore, ranges are provided instead of single values. IFOV, instantaneous field of view. DoD, United States Department of Defense.

Satellite	Sensor	IFOV at Nadir (km)	Revisit Time	Agency	Temporal Coverage	Source
GOES 1–19	VISSR, VAS, Imager, ABI	2–6.9 (IR)	15–30 min	NOAA/ NASA	1975–present	https://www.goes-r.gov/products/samples.html (accessed on 1 December 2024)
Meteosat 1–11 (MOP/ MSG/MTG)	MVIRI, SEVIRI	3–5 (IR)	15–25 min	ESA/ EUMETSAT	1977–present	https://space.skyrocket.de/directories/sat_met_eur.htm (accessed on 1 December 2024)

Table 2. *Cont.*

Satellite	Sensor	IFOV at Nadir (km)	Revisit Time	Agency	Temporal Coverage	Source
Himawari (GMS/ MTSAT)	VISSR, JAMI, Imager, AHI	2–5 (IR)	10–30 min	JMA/JCAB/ JAXA	1977–present	http: //www.data.jma.go.jp/mscweb/en/index.html (accessed on 18 Decem-ber 2024)
FY	VISSR-1/2, AGRI	4–5.76 (IR)	15–30 min	CMA/ NRSCC	1997–present	http://data.nsmc.org.cn/DataPortal/en/home/index.html (accessed on 1 December 2024)
DMSP	SSM/I, SSMIS	11–73 km (19–183 GHz), 28 × 37 km (37 GHz), 13 × 15 km (85 GHz)	×	DoD/NOAA	1987–present	https://rammb.cira.colostate.edu/dev/hillger/DMSP.html (accessed on 1 December 2024)
TRMM	TMI	4–37 km (10–86 GHz)	×	NASA/ JAXA	1997–2015.04	https://gpm.nasa.gov/missions/TRMM/satellite (accessed on 1 December 2024)
	PR	5 km (13.8 GHz)				
NOAA	AMSU-B, MHS, ATMS	16–75 km (23–183 GHz),	×	NASA/ NOAA	1998–present	https://www.nesdis.noaa.gov/our-satellites/related-information/history-of-noaa-satellites (accessed on 1 December 2024)
Aqua	AMSR-E	4–75 km (6.9–89 GHz)	×	NASA	2002.06–2011.10	https://aqua.nasa.gov/content/amsr-e (accessed on 1 December 2024)
METOP	MHS(A–C)	16 × 16 km (89–190 GHz)	×	EUMETSAT/ ESA	2006–present	https://space.skyrocket.de/doc_sdat/metop.htm (accessed on 1 December 2024)
S-NPP	ATMS	16–75 km (23–183 GHz)	×	NASA/ NOAA	2011–present	https://rammb.cira.colostate.edu/projects/npp/ (accessed on 1 December 2024)
Megha-Tropiques	SAPHIR	10 × 10 km (183 GHz)	×	CNES/ ISRO/	2011–present	https://space.skyrocket.de/doc_sdat/megha-tropiques.htm (accessed on 1 December 2024)
GCOM-W1	AMSR-2	3–62 km (7–89 GHz)	×	JAXA	2012–present	https://suzaku.eorc.jaxa.jp/GCOM_W/w_amsr2/amsr2_body_main.html (accessed on 1 December 2024)
GPMCO	GMI	4–32 km (10–183 GHz)	×	NASA/ JAXA	2014–present	https://gpm.nasa.gov/missions/GPM (accessed on 1 December 2024)
	DPR	5 × 7 km (13.6, 36.5 GHz)				

Launched in 1997, the TRMM primarily focused on quantifying atmospheric parameters over tropical and subtropical oceans based on the onboard microwave imager (TMI) and PR at 13.8 GHz [73]. The TRMM officially concluded its mission on 15 April 2015. The GPMCO, launched in 2014 as an extension of TRMM [20], represents a significant advancement in the field. It offers enhanced capabilities for measuring light rain (<0.5 mm/h), solid precipitation, and the microphysical properties of precipitating particles. The onboard Ka-band (35.5 GHz) and Ku-band (13.6 GHz) PR enable a three-dimensional measurement of precipitation structures. The Ka/Ku-band DPR can offer novel insights into particle drop size distributions during moderate precipitation [74]. Thus, it establishes the current standard for spaceborne precipitation estimation.

The GPM mission conducts high-precision global precipitation measurements every 0.5–3 h [20]. It consists of a constellation of satellites equipped with PMW sensors from the space agencies of the USA, Japan, Europe, and India (Figure 2). Each member contributes PMW measurements to the mission for generating uniformly processed global precipitation products. The GPM mission has played a crucial role in the advancement of MPE [75]. By utilizing updated sensors, more recent periods can expect higher-resolution and better-quality precipitation datasets.

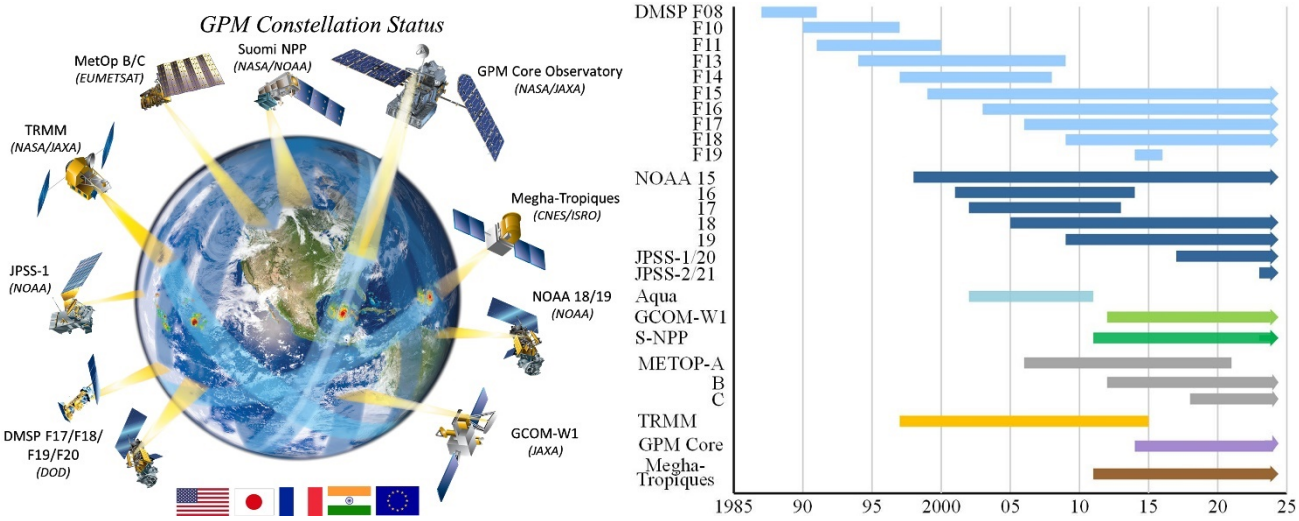

Figure 2. GPM constellation. The left figure was obtained from https://gpm.nasa.gov/image-gallery/gpm (accessed on 1 December 2024).

3. Physical Basis of Multi-Sensor Precipitation Estimation

3.1. IR-Based Precipitation Estimation

IR observations are indirectly linked to precipitation. The fundamental physical principle is that precipitation is predominantly associated with deep clouds and, consequently, cold cloud tops. The lower cloud-top temperature serves as an indicator of precipitation occurrence. However, it should be noted that this relationship does not necessarily hold [76]. The GOES Precipitation Index (GPI) [69] and the GOES Multi-Spectral Rainfall Algorithm (GMSRA) [70] represent typical examples of IR-based techniques employed in this context. These IR-based approaches perform relatively favorably when applied to larger spatiotemporal scales [17].

3.2. PMW-Based Precipitation Estimation

PMW observations are physically linked to precipitation. PMW sensors capture the upwelling MW radiation emitted from the Earth's surface, which is then attenuated by the atmosphere. Precipitation particles are the main source of attenuation. The emission of radiation from precipitation particles results in an increase in the signal, while the scattering due to hydrometeors reduces the radiation. The type and size of the hydrometeors detected by PMW sensors depend on the frequency of the upwelling radiation. Above 85 GHz, ice scattering dominates. Below about 22 GHz, absorption is the primary mechanism affecting the transfer of MW radiation. Between 19.3 and 85.5 GHz, the common PMW sensor channel range (such as 19.35, 22.235, 37.0, and 85.5 GHz), radiation interacts with the main types of hydrometeors, water particles or droplets (liquid or frozen).

Over oceans, the background microwave signals remain constantly low (emissivity, ε, ~0.4–0.5), and the presence of precipitation (ε = ~0.8) enhances the microwave signals. The enhanced signals can be decomposed to retrieve precipitation at low-frequency bands (<20 GHz). Land surface emissivities, however, are heterogenous in space and comparable in magnitude to precipitation (ε = 0.7–0.9), challenging the accurate retrieval of precipitation. Additionally, the presence of ice particles causes a reduction in microwave signals at frequencies >35 GHz as a result of scattering effects [77,78]. In addition, high-frequency PMW observations (about > 183 GHz) can provide the ability to retrieve precipitation over regions such as coastlines and areas with snow/ice. Thus, PWV-based precipitation estimation involves two distinct processes: emission from rain droplets and scattering by precipitating ice particles.

Several PMW-based approaches have been proposed considering the two processes. Ferraro [71] developed a statistical–physical algorithm that considers the scattering effects at

85 GHz over land, which was additionally combined with the emissions at 19/37- GHz over oceans. This algorithm was mainly applied in the Special Sensor Microwave/Imager (SSM/I) and Special Sensor Microwave Imager/Sounder (SSMIS). Kummerow et al. [79,80] proposed the GPROF algorithm, based on Bayesian theory. This Bayesian approach was used to create an a priori database of observed cloud and the hydrometeor profiles. GPROF has undergone significant evolution and enhancement since Randel et al.'s work [81–85]. The framework of the GPROF algorithm was adapted for the TRMM and later the GPM imagers and constellation satellites. Hilburn and Wentz [86] proposed the Unified Microwave Ocean Retrieval Algorithm (UMORA) based on the over-ocean rainfall retrieval algorithm [87]. It uses the 19 and 37 GHz observations that are common to a wide variety of PMW sensors (GMI, TMI, SSM/I, and SSMIS). Boukabara et al. [88] developed the Microwave-Integrated Retrieval System (MiRS) algorithm based on a one-dimensional variational methodology. It retrieves the physical attributes affecting MW observations, including the profile of atmospheric water vapor and hydrometeors. The MiRS has been applied to PMW sensors, such as the Advanced Microwave Sounding Unit (AMSU)/the Microwave Humidity Sounder (MHS), SSMIS, Suomi National Polar-orbiting Partnership (S-NPP), Advanced Technology Microwave Sounder (ATMS), and Sounder for Atmospheric Profiling of Humidity in the Intertropics by Radiometry (SAPHIR) (Megha-Tropiques).

3.3. AMW-Based Precipitation Estimation

AWV observations are more direct and effective in estimating precipitation from space. A precipitation radar (PR) emits a microwave signal that interacts with precipitation, measuring the backscatter portion of this signal that returns to the sensor. The received power of the radiation backscatter from precipitation is generally proportional to the number of particles in the size range of precipitation, thus reflecting its intensity. Typically, radar-derived precipitation intensity is associated with the reflectivity factor, which is determined logarithmically. However, this relationship does not hold universally, depending on factors such as particle size, shape, orientation, and to some extent phase.

The standard PR algorithm estimates the effective reflectivity factor (Ze) at 13.8 GHz (Ku band) from the vertical profiles of the measured reflectivity factor. Subsequently, the rainfall rate is calculated based on the estimated Ze value [89]. One major source of error stems from the variations in raindrop size distribution (DSD) [90]. The DPR algorithm aims to estimate profiles of precipitation water content, rainfall rate, as well as particle size distribution in both rain and snow [91]. The introduction of an additional Ka band (35.5 GHz) for DPR was motivated by multiple factors. It provides DSD information from non-Rayleigh scatters and enhances the accuracy of phase-transition height estimation in precipitating systems. Additionally, it improves the detection of snow events at higher latitudes. The Level-1 DPR algorithm is independently applied to KuPR and KaPR data [92], whereas the Level-2 DPR algorithms comprise three versions: KuPR, KaPR, and dual-frequency algorithms [93–95].

4. Combining MPE Methodologies

To enhance the spatiotemporal coverage of precipitation data, it is necessary to merge retrievals from multiple similar sensors (e.g., [25,26,96] for PMW and [97] for IR). In this review, we primarily focus on MPE, i.e., merging precipitation and/or cloud information from both PMW and IR observations.

4.1. Probability Matching Method

The probability matching method (PMM) was initially proposed to establish reflectivity–rain rate relationships for radar data by utilizing cumulative density functions [98,99]. Barrett et al. [100] observed that the overestimated rainfall retrievals were caused by the low rain-rate skew and thus suggested employing cumulative histograms to correlate ground rainfall observations with satellite estimates. Manobianco et al. [101] calibrated the IR Tb threshold (rain/non-rain) based on occasional precipitation estimates obtained from PMW

data using the cumulative histogram matching method. The combined passive microwave–infrared (PMIR) algorithm, as described by Kidd et al. [17] and Kidd and Muller [102], utilizes a cumulative histogram matching approach to establish an IR Tb–PMW–rain-rate relationship, enabling the provision of PMW-calibrated IR estimates of precipitation. This algorithm operates under the assumption that colder clouds are associated with higher rainfall amounts compared to warmer clouds, indicating a monotonically increasing precipitation rate with decreasing Tb. Additionally, it assumes that the IR Tb exhibits a similar cumulative frequency as the PMW precipitation estimate at specific spatial and temporal scales. The equations expressing the PMM are as follows.

$$C_1(Tb_{IR}) = \int_{Tb_1}^{Tb} f_1(Tb_{IR})dTb \quad (1)$$

$$C_2(P_{PMW}) = \int_{PMW_1}^{PMW} f_2(P_{PMW})dP_{PMW} \quad (2)$$

$$C_2^{-1}[C_1(Tb_{IR})] \xrightarrow{f_3} Tb_{IR} \quad (3)$$

where P_{PMW} is the precipitation rate retrieved based on PMW; $f_1(Tb_{IR})$ and $f_2(P_{PMW})$ are the probability density functions of IR Tb and P_{PMW}, respectively; $C_1(Tb_{IR})$ and $C_2(P_{PMW})$ are the cumulative density functions of IR Tb and P_{PMW}, respectively; and f_3 represents the relationship between P_{PMW} and IR Tb. The frequency histograms of P_{PMW} and IR Tb are generated and converted into cumulative histograms before being matched, so that the occurrence of the heaviest precipitation is associated with the Tb values linked to the heaviest rainfall. A Tb–P_{PMW} functional relationship between PMW precipitation rates and IR Tb is established for certain spatiotemporal ranges. Moreover, the rain–no-rain threshold is defined; this threshold greatly affects the final precipitation estimation. Finally, the Tb and P_{PMW} functions are applied to GEO IR Tb (below the rain–no-rain threshold), and the final precipitation rates are then obtained.

The PMM has been successfully applied to derive global hourly satellite precipitation products. It has also found extensive application in various algorithms for integrating IR Tb and PMW estimates, including the algorithm proposed by Anagnostou et al. [103], the Microwave/Infrared Rain Algorithm (MIRA) [104], the MW–IR Combined Rainfall Algorithm (MICRA) [105,106], the PERSIANN Cloud Classification System (PERSIANN-CCS) [29], the Naval Research Laboratory Blended (NRLB) algorithm [107], and the CMORPH Climate Data Record (CMORPH CDR) [108]. Among these algorithms, there is significant variation in defining the rain–no-rain threshold. For example, Kidd et al. [17] defined this threshold as the Tb value corresponding to the same cumulative frequency as that of non-rain events determined from PMW estimates. MIRA employs spatially and temporally varying optimal IR rain/no-rain thresholds derived through calibration against rain gauge observations [104]. Furthermore, in addition to its applications in precipitation product generation, PMM can also be utilized for downscaling purposes [109].

4.2. Cloud-Motion-Based Method

Given the accurate measurements of cloud-top motion provided by IR data, these observations can be effectively utilized for cloud system detection and tracking. The pioneering work by Joyce et al. [26] introduced the Cloud Motion-based Precipitation Estimation (CMORPH) method to estimate global precipitation patterns. This approach assumes a linear evolution of precipitation between successive PWV images and considers constant precipitation intensity during both the forward and backward propagation of PMW estimates. By leveraging cloud movement, PMW-derived rainfall is advected or morphed across satellite overpasses, accounting for changes in intensity and shape through the

inverse weighting of forward- and backward-propagated rainfall values. The computation process for obtaining morphed values is as follows:

$$\text{value}_{(t+1/\text{n}*\text{h})} = w1 \times p_{forward(t+1/\text{n}*\text{h})} + w2 \times p_{backward(t+1/\text{n}*\text{h})} \quad (4)$$

$$\text{value}_{(t+2*1/\text{n}*\text{h})} = w2 \times p_{forward(t+2*1/\text{n}*\text{h})} + w1 \times p_{backward(t+2*1/\text{n}*\text{h})} \quad (5)$$

where $w1$ and $w2$ are weight coefficients, and 1/n represents the temporal resolution of the retrieval. Instantaneous PMW rainfall (time = t) is propagated forward to produce analyses at t + 1/n*h ($P_{forward(t+1/\text{n}*\text{h})}$) and t + 2*1/n*h ($P_{forward(t+2*1/\text{n}*\text{h})}$) using the IR-derived cloud vector. Meanwhile, the instantaneous PMW rainfall (time = t + 3*1/n*h) is propagated backward to produce analyses at t + 2*1/n*h ($P_{backward(t+2*1/\text{n}*\text{h})}$) and t + 1/n*h ($P_{backward(t+2*1/\text{n}*\text{h})}$). It is noted that the 3 in the numerator inherently assumes a 3*1/n-hour time gap between PMW retrievals. In the CMORPH algorithm, $w1$ and $w2$ are 0.67 and 0.33, respectively, and 1/n is 0.5 h. The arly CMORPH versions used the IR-derived cloud vector directly to propagate PMW precipitation. To correct advection rates, a speed- adjustment procedure was subsequently developed by first computing rainfall advection vectors using spatially lagging hourly U.S. NEXRAD stage-II radar rainfall data. The IR-derived cloud vectors were then synthesized to an hourly frequency to match that of the radar-derived rainfall vectors.

A potential primary source of error in this algorithm lies in the fact that the advection analysis solely accounts for the temporal variation in the precipitation system. To address this, a Kalman filter (KF) was employed to enhance feedback information and more accurately represent the temporal variation in the precipitation system [110]. Consequently, a KF-model-based algorithm (GSMaP_MVK) was developed to refine the propagated precipitation rate based on cloud vectors. Specifically, a KF was applied to propagate rainy pixels, and the same propagation and KF procedure were utilized during backpropagation of these pixels. At time t, when the PMW sensor passes over, the rainy pixel undergoes repeated propagation, and the Kalman Filter (KF) updates the precipitation rate as ${R^f}_{t,i}$ after i hours. The rainy pixels that are revisited undergo repeated backward propagation, while the precipitation rate is updated by the KF as ${R^b}_{t,j}$, equal to the estimated precipitation rate j hours before the most recent PMW sensor overpass (t + hour time gap between PMW retrievals). In this case, the optimal estimate R is defined with the following equation:

$$\hat{R} = {R^f}_{t,i}\frac{\sigma_j}{\sigma_j + \sigma_i} + {R^b}_{t,j}\frac{\sigma_i}{\sigma_j + \sigma_i} \quad (6)$$

where σ is the root mean square uncertainty in the estimates i or j hours after the PMW overpass.

Joyce and Xie [111] further enhanced the KF-based CMORPH algorithm, which incorporates both forward and backward propagation of PMW estimates from their observation times to the target analysis time (final retrieval time). The forecast at the analysis time is then determined by averaging the forward- and backward-propagated PMW estimates, weighted inversely according to their error variances. However, unlike the GSMaP_MVK algorithm, this KF model relies solely on propagating PMW estimates for precipitation forecasting without considering the changes in the pattern or intensity of precipitating systems. The GPM IMERG algorithm also utilizes the KF model [30,112]. Additionally, Behrangi et al. [113] proposed the REFAME method, which incorporates a forward-adjusted advection of microwave estimates to construct high-resolution precipitation analyses. In this algorithm, PMW estimates are propagated along motion vectors defined by 2D cloud tracking while accounting for intensity changes during the propagation process.

4.3. Adjustment-Ratio-Based Method

A technique based on the adjustment ratio (AR) was proposed to calibrate or adjust the rain rates inferred from GEO IR data using PMW estimates [114]. It is assumed that PMW-based estimates provide accurate instantaneous precipitation but have limited

spatial and temporal sampling, while IR estimates offer extensive spatial coverage and sampling frequencies but contain significant systematic errors. The objective is therefore to generate rainfall estimates superior to either of these individual approaches. The AR can be calculated based on coincident PMW and IR data by employing the following equations:

$$P_{\mathrm{PMW}} = f_4(Tb_{\mathrm{PMW}}) \tag{7}$$

$$P_{\mathrm{IR}} = f_5(Tb_{\mathrm{IR}}) \tag{8}$$

$$\mathrm{AR} = \frac{P_{\mathrm{PMW}}}{P_{\mathrm{IR}}} \tag{9}$$

where Tb_{PMW} represents a cloud parameter derived from PMW (e.g., the Scattering Index in Ferraro's work); P_{IR} represents the precipitation rate estimated based on the coincident IR; $f_4(Tb_{\mathrm{PMW}})$ represents the relationship between P_{PMW} and Tb_{PMW} (e.g., the Goddard Scattering Algorithm); and $f_5(Tb_{\mathrm{IR}})$ represents the relationship between P_{IR} and Tb_{IR} (e.g., GPI). It is thus necessary to ensure that PMW and IR are constructed from nearly coincident data. In addition, it is necessary to use a moving average (e.g., 5×5 grid box) before calculating the ARs to produce a smooth field of coefficients. Finally, the spatial array of ARs is then multiplied by the original IR estimates to produce the calibrated estimates using a simple assigned threshold technique (235 K).

The AR-based method is commonly employed for obtaining monthly precipitation estimates, such as those acquired using the adjusted GPI (AGPI) algorithm [115]. AGPI utilizes matched PMW and GEO IR datasets to generate an AR map that can subsequently be applied to IR precipitation estimate fields in order to produce adjusted estimations. All the available IR data can then be utilized for obtaining precipitation estimates, while a secondary IR-based mean of precipitation can be constructed solely using the spatiotemporally corresponding IR data during PMW overpasses. The AGPI algorithm preserves the typically low bias of PMW estimates along with ensuring smoothness and temporal coverage from GEO IR data. The AGPI was successfully employed to construct global monthly precipitation analyses for the Global Precipitation Climatology Project (GPCP) [116–119]. Additionally, during the production process, small fractions were utilized to generate pentad and daily precipitation analyses. Subsequently, Kummerow and Giglio [120] as well as Xu et al. [121] developed more sophisticated approaches based on AGPI, termed by the latter as the Universally AGPI (UAGPI) method, wherein the optimization of the IR threshold $f_2(Tb_{\mathrm{IR}})$ is incorporated. Furthermore, the AR method can be applied to adjust satellite precipitation estimates using gauged data (e.g., [25,122]).

4.4. Neural-Network-Based Method

The artificial neural network (ANN) structure has been mathematically proven to be a universal function approximator, and these networks possess the ability to intelligently "learn" functions through an automated training process. The fundamental form of an ANN is referred to as a multilayer feedforward network. Hsu et al. [28] developed an adaptive method based on a modified counter propagation network (MCPN), which represents a hybrid three-layer network comprising two components. The input hidden layer transformation constitutes a self-organizing feature map (SOFM) that identifies and categorizes patterns in the input data. The hidden– output layer transformation involves an enhanced version of the Grossberg linear layer, which calculates a specific precipitation rate for each input pattern. The nodes in the hidden layer are typically organized in a square matrix configuration. Initially, the SOFM parameters undergo training via an "unsupervised" self-organizing clustering procedure. Subsequently, the parameters of the hidden output layer are trained using a "supervised" process based on a simple recursive gradient search.

To utilize the MCPN model effectively, it is necessary to specify the input–output data and determine the number of nodes. In the PERSIANN algorithm, the network structure comprises six normalized input variables derived from GEO IR and 225 nodes arranged

in each matrix within the hidden and output layers [28]. An adaptive procedure is employed for the recursive updating of network parameters when ground-based data become available. Sorooshian et al. [123] enhanced the PERSIANN algorithm by incorporating PMW data to ensure regular updates of network parameters. To address a limitation of PERSIANN—which relies on local pixel information for rainfall estimation—Hong et al. [29] developed the PERSIANN-CCS algorithm. The algorithm encompasses a segmentation step applied to GEO IR cloud images, the extraction of cloud features, the classification of cloud patches, and the calibration of Tb and rainfall relationships. Additionally, this algorithm can be utilized for obtaining the PERSIANN-CCS-CDR dataset. PERSIANN-CCS precipitation is employed by the IMERG algorithm.

In comparison to a conventional ANN, a deep neural network (DNN) is characterized by an increased number of hidden layers, which enable it to provide enhanced classification and regression capabilities [124,125]. Tang et al. [126] developed a DNN-based approach for estimating rain and snow rates at high latitudes. Their method leverages the precipitation estimates derived from spaceborne radars to train using PMW and IR Tb data along with reanalysis environmental variables. Moreover, DNNs were trained based on various scenarios of combined channels, such as combinations of 6.2 μm, 7.3 μm, 10.8 μm, and 12 μm and of 0.6 μm and 10.8 μm.

4.5. Weighted-Average-Based Method

Xie and Arkin [127] proposed a maximum likelihood estimation method based on the weighted average approach to combine diverse observations. The weighting coefficients in this procedure are inversely proportional to the squares of individual random errors, which are determined by comparing the errors with gauge observations and subjective assumptions. This methodology assumes that (1) each type of observation error Pi is random, unbiased, and normally distributed and (2) the observation errors σ_i are independent across different types of observations. The maximum likelihood estimate for *C* is defined by the following equations:

$$C = \sum W_i P_i \tag{10}$$

$$W_i = \frac{\sigma_i^{-2}}{\sum \sigma_i^{-2}} \tag{11}$$

Xie and Arkin [127] linearly merged the estimates from infrared (IR) data (GPI), microwave scattering-based data (Grody), microwave emission-based data (Chang), and numerical model predictions (ECMWF). Theoretically, a linear combination of these estimates results in smaller random errors compared to individual estimates; however, the biases present in the individual datasets persist in the combined analysis. To address these limitations, the authors developed a stepwise strategy to reduce both the random errors in the individual sources and the bias in the combined analysis. This methodology was successfully applied to create the CPC Merged Analysis of Precipitation (CMAP) [128], which integrates gauge observations, satellite-derived estimates, and National Center for Environmental Prediction-National Center for Atmospheric Research (NCEP-NCAR) reanalysis data. Huffman et al. [116] employed a weighted average method to combine AGPI estimates with rain gauge analysis and Numerical Weather Prediction (NWP) model precipitation data. Similar methods have also been utilized in other GPCP precipitation products [117–119].

4.6. Regression-Based Method

The regression-based approach assumes a relationship between PMW estimates and IR channels. The general description of PPMW can be formulated based on the following equation:

$$P_{\mathrm{PMW}} = f_6(Tb_{\mathrm{IR}}) \tag{12}$$

where Tb_{IR} is derived from an IR channel or multiple channels, and $f_6(Tb_{IR})$ represents the relationship between P_{PMW} and Tb_{IR}. More specifically, a regression-based technique can be described in which PMW-derived precipitation is used to adjust the basic relationship between IR Tb and surface rain rates.

Vicente and Anderson [129] employed a multiple linear regression approach to establish the relationship between SSM/I-based precipitation estimates and Tb10.7 values for all GOES pixels within a given SSM/I pixel. The IR Tb data were divided into distinct intervals, and separate equations were developed for each interval to enhance the technique's capability to handle nonlinearity. Miller et al. [130] proposed the microwave/infrared rain rate algorithm (MIRRA) to calibrate both a minimum T10.7 rain/no-rain threshold and a regression-based relationship with the rain rate by regressing against the minimum T10.7 value. The SCaMPR algorithm proposed by Kuligowski et al. [131] offers a self-calibrating approach for multivariate precipitation retrieval, specifically designed for short-term flash flood forecasting applications. This algorithm enables real-time calibration of an optimal rain-rate predictor (e.g., GMSRA) against PMW precipitation through linear regression, allowing for the identification of raining pixels and the selection of optimal predictors to delineate rain areas separately.

$$P_{PMW} = \mathrm{a} \times f_7(Tb_{IR}) + \mathrm{b} \tag{13}$$

where $f_7(Tb_{IR})$ is a precipitation predictor calculated from the difference between IR channels (Tb, 6.9–12.0 μm), such as GPI, GMSRA, and the autoestimator [132]. In essence, this approach is similar to the multiple linear regression method. Kuligowski et al. [133–135] further added some modifications (e.g., an additional PMW source) to SCaMPR. The regression-based method has not been used to obtain global precipitation thus far. At present, this method is often used to obtain regional precipitation estimates.

5. Satellite Precipitation Products

The development of satellite SPPs is sensor-dependent, particularly those within the GPM constellation. During the initial phase, most products (e.g., GPCP and CMAP) are released on coarse spatiotemporal resolutions (2.5°, monthly). The launch of the TRMM and the improvements in satellite sensors thereafter have enabled the quasi-real-time generation of high-resolution (e.g., better than 0.25°, 3 h) global precipitation datasets. The High-Resolution Precipitation Products (HRPPs) such as TMPA, CMORPH, GSMaP, PERSIANN, and IMERG were subsequently generated. Currently, precipitation data are available at various spatiotemporal resolutions to cater to diverse user requirements. Figure 3 provides an overview of the major satellite precipitation products currently accessible.

5.1. Precipitation Products with Low Spatiotemporal Resolution

The GPCP dataset (V2.3) comprises monthly (2.5° × 2.5°), pentad (2.5° × 2.5°), and daily (1° × 1°) products. The monthly product is generated based on the weighted average-based method and AR-based method [117]. Subsequent enhancements have been periodically implemented over the years [118,119,136]. The daily product [137] is accessible from late 1996 onward, while the pentad product [138] covers the period from 1979 to present. These GPCP products can be obtained from National Oceanic and Atmospheric Administration (NOAA) National Centers for Environmental Information (NCEI) via WMO's World Data Center website (https://www.nccs.nasa.gov/services/data-collections/atmosphere-based-products/gpcp, accessed on 1 December 2024).

The CMAP dataset comprises monthly precipitation (2.5° × 2.5°) and pentad precipitation (2.5° × 2.5°). This dataset integrates estimates from diverse satellite observations, monthly gauge analyses from the Global Precipitation Climatology Centre (GPCC) and the Global Historical Climatology Network (GHCN), as well as precipitation data from the NCEP–NCAR reanalysis using a weighted-average-based approach [127,128]. These CMAP products can be accessed through the Earth System Research Laboratory at NOAA

(https://www.cpc.ncep.noaa.gov/products/global_precip/html/web.shtml, accessed on 1 December 2024).

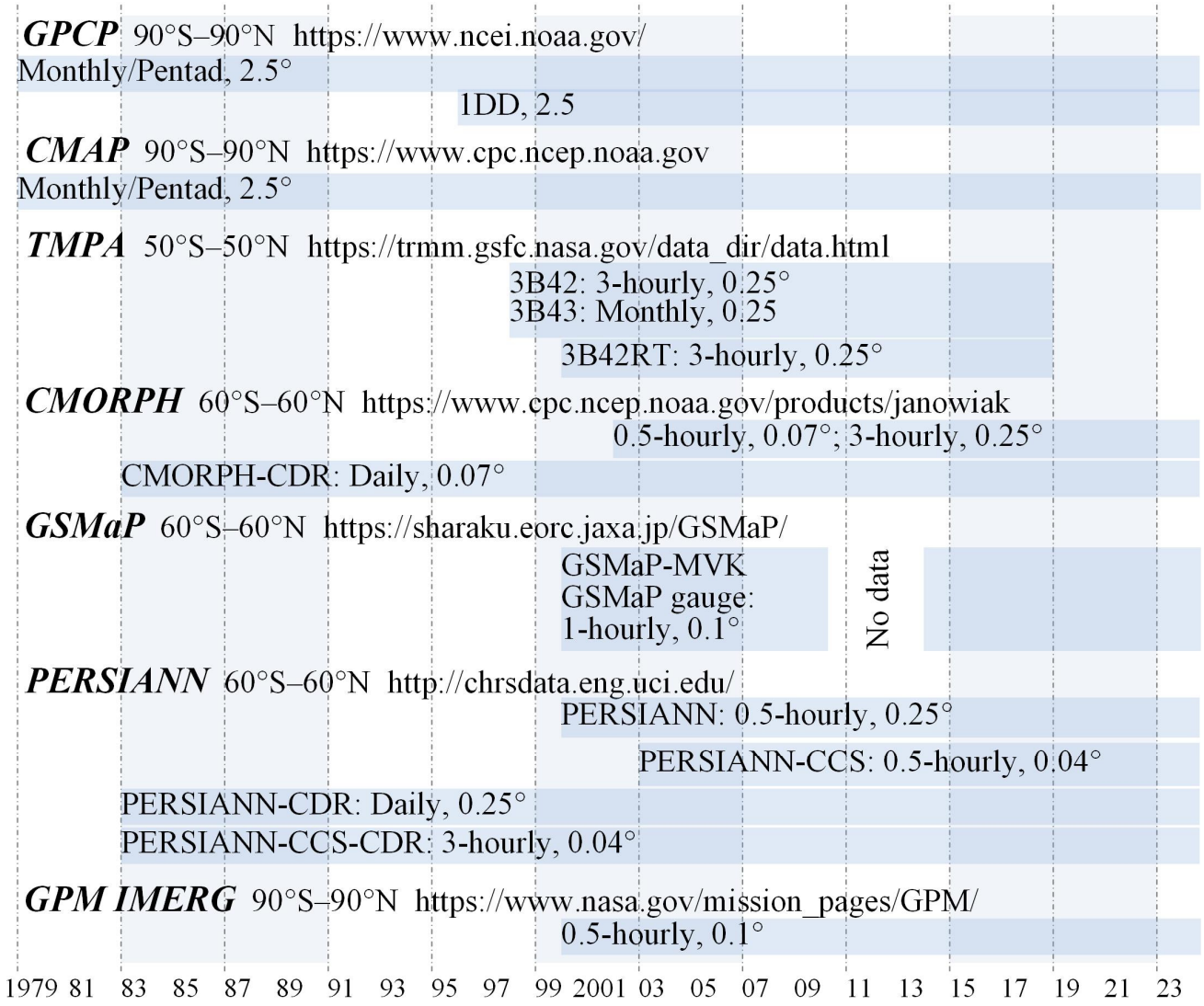

Figure 3. Summary of major global satellite precipitation products currently available.

5.2. Precipitation Products with High Spatiotemporal Resolution

The TMPA comprises the TRMM 3B42RT (0.25°/3 h) and 3B43 (0.25°/monthly) products. The TMPA algorithm integrates IR estimates and PMW retrievals through a series of adjustments and combinations, including calibration of IR brightness temperatures using PMW retrievals (via PMM), merging of PMW and IR estimates to generate TRMM 3B42RT, and rescaling the results to monthly totals for unadjusted TRMM 3B43 [25]. To optimize accuracy, both TRMM 3B42 and 3B43 datasets are corrected using global monthly rain gauge data. The PMW data primarily originated from sensors such as TMI (GMI after the retirement of TRMM), SSM/I/SSMIS, AMSR-E (AMSR2 after 2012), AMSU-B, and MHS. The Precipitation Process System within NASA's Earth Observing System Science and Data Information System was responsible for producing the TMPA dataset at ftp://trmmopen.gsfc.nasa.gov/pub/merged (accessed on 28 October 2020). Notably, the TMPA was retired at the end of 2019.

The IMERG currently comprises a 0.1°/0.5 h product. The GPM IMERG algorithm aims to intercalibrate, merge, and interpolate satellite PMW precipitation estimates with PMW-calibrated IR estimates, gauge data, and potentially other precipitation estima-

tors [30]. This algorithm incorporates various methods employed in global precipitation estimation algorithms such as the cloud-classification method in PERSIANN-CCS [28], the KF-based CMORPH algorithm [111], and the PMM-based method. While the core algorithm is based on KF-based CMORPH, additional methods are utilized to enhance and adjust the IR and PMW estimates. The production of the GPM dataset is overseen by PPS in EOSSDIS at NASA (available at https://pmm.nasa.gov/data-access/downloads/gpm, accessed on 1 December 2024). Notably, the GPM IMERG extends its temporal coverage to include the TRMM era and now offers a 20-year-long data series spanning from 2000 to the present [139].

The CMORPH comprises products with spatial resolutions of 0.25°/3 h, 0.07°/0.5 h, and CDR (0.07°/daily). The CMORPH algorithm integrates passive microwave (PMW) and infrared (IR) data through a cloud-motion-based approach [26], which is further enhanced using a Kalman filter model [111]. PMW observations are obtained from diverse sources including SSM/I, SSMI/S, AMSU-B, AMSR-E, and GMI sensors. Cloud vectors are corrected using radar data from the U.S. Next-Generation Weather Radar (NEXRAD) stage-II product. Xie et al. [108] reprocessed the satellite-based CMORPH precipitation estimates and rectified biases by incorporating gauge data via the Precipitation Measurement Mission (PMM), resulting in the creation of the CMORPH CDR dataset. The Climate Prediction Center (CPC) of the NOAA is responsible for generating the CMORPH datasets.

The GSMaP comprises 0.1°/1 h near-real-time products (GSMaP_NRT, GSMaP_Gauge_NRT), 0.1°/1 y standard products (GSMaP_MVK, GSMaP_Gauge), and a 0.1°/0.5 h real-time satellite precipitation product (GSMaP-NOW). GSMaP_NRT is derived from the MW-IR merged data (GSMaP_MVK), excluding backward propagation to provide near-real-time information, while GSMaP_Gauge_NRT represents the corresponding gauge-based adjusted product [86,140]. The GSMaP_MVK algorithm applies a Kalman filter model to refine the PMW estimates obtained through cloud-motion-based methods [110]. Additionally, GSMaP_Gauge is a rain-gauge-adjusted product based on GSMAP_MVK [141]. The GSMaP-NOW, produced using the GSMaP V06 algorithm, has been available for the whole globe since June 2019 [110,142]. PMW data are acquired from various Microwave Imager sensors including GMI, SSM/I, AMSR-E, AMSR2, and MADRAS sensors; IR data are provided by NCEP/CPC. Currently, the Precipitation Measuring Mission (https://sharaku.eorc.jaxa.jp/GSMaP_NOW/index.htm, accessed on 1 December 2024) offers access to the GSMAP products through its Science Team at JAXA.

The PERSIANN currently comprises the following products: PERSIANN (0.25°/1 h), PER-SIANN-CCS (0.04°/1 h), PERSIANN-CDR (0.25°/daily), and PERSIANN-CCS-CDR (0.4°/3 h). The precipitation estimation algorithm employed by PERSIANN utilizes an artificial neural network-based approach that incorporates infrared-imagery-derived cloud information, adjusted using passive microwave data [28,123]. The PERSIANN-CDR product is an infrared-based climate monitoring product trained using radar data and normalized to GPCP monthly totals [143]. The estimation of precipitation in the PERSIANN CCS product involves establishing distinct relationships between infrared brightness temperature and precipitation through the use of PMM; these estimates are further calibrated using co-located cloud images and gauge-corrected radar rainfall data corresponding to each classified cloud group [29]. Finally, the generation of the PERSIANN-CCS-CDR product begins with the rain rate outputs from the PERSIANN-CCS model, which are subsequently adjusted using GPCP V2.3 [144]. The production of the comprehensive PERSIAN dataset is carried out by the Center for Hydrometeorology and Remote Sensing (CHRS) at the University of California, Irvine (http://chrsdata.eng.uci.edu/ accessed on 1 December 2024).

6. Validation

Satellites do not measure precipitation. Instead, they capture sensor-dependent quantities, which are further converted to precipitation rates [69,79]. The conversion processes can introduce significantly varying errors among SPEs [145]. Consequently, the rigorous

validation of SPEs becomes indispensable, as it is a prerequisite to enhance the quality of SPEs and ultimately advance their applicability across diverse domains [146,147].

6.1. Validation Practices for Satellite Precipitation

The World Climate Research Programme (WCRP) conducted three Algorithm Intercomparison Projects (AIPs) in 1986 [22,23,148]. These AIPs aimed to evaluate the performance of the available algorithms for IR, PMW, and MPE. Simultaneously, the WetNet Project organized three Product Intercomparison Projects (PIPs) [149–153]. These PIPs were designed to assess the accuracy of SPEs and determine the optimal algorithm. Both the AIPs and PIPs evaluated SPEs primarily at relatively low resolutions (0.5° × 0.5°, 2.5° × 2.5°, and 5° × 5°) from various perspectives. The AIPs prioritized algorithm performance, while the PIPs focused on accuracy and application. In 2007, the WMO implemented the Program to Evaluate High-Resolution Precipitation Products (PEHRPP) (<3 h, <0.25°) [55,154]. The primary objective of PEHRPP was to comprehensively assess the errors in various high-resolution precipitation products across different spatial and temporal scales, as well as diverse underlying surfaces and climatic conditions. The PEHRPP evaluations primarily covered Australia [155], the United States [155,156], Europe [155], and India [157]. Additionally, the GPM Cold Season Precipitation Experiment (GCPEX), a collaborative effort between NASA's GPM ground validation program and its international partner Environment Canada, aimed to provide new datasets and insights into snowfall processes for enhancing falling-snow retrievals [158,159].

Alongside these programs, the International Precipitation Working Group (IPWG), which is jointly sponsored by the Coordination Group for Meteorological Satellites (CGMS) and the WMO, placed significant emphasis on the verification, validation, and intercomparison of SPPs in 2002 [61,63,65]. The Precipitation Virtual Constellation (P-VC) within the Committee on Earth Observation Satellites (CEOS) also focused on comparing and evaluating different SPPs in 2019. Furthermore, a Joint IPWG-GDAP Precipitation Assessment report was released by IPWG and GEWEX Data and Analysis Panel (GDAP) to assess precipitation products [57]. Additionally, numerous studies have evaluated the performance of SPPs over the past two decades (Figure 4).

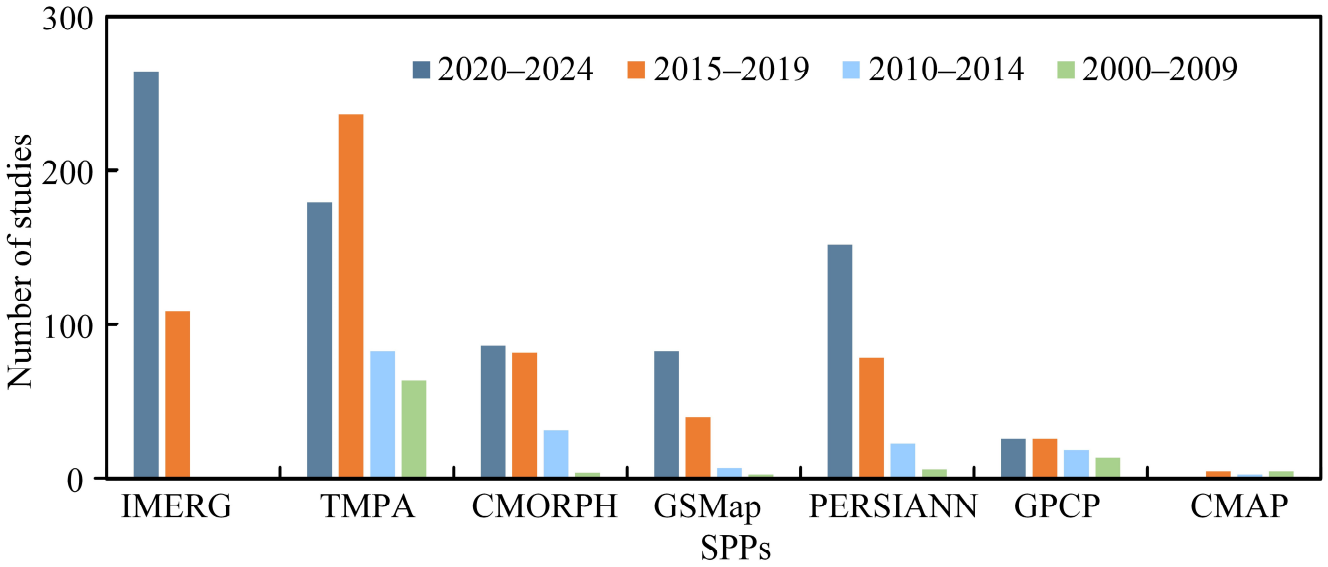

Figure 4. Number of SPP validation studies published over the last two decades (covered in Web of Science Core Collection). We used the keywords "validation" or "evaluation" or "assessment" for the topic and "IMERG", "PERSIANN", "CMORPH", "GSMaP", "CMAP and Merged Analysis of Precipitation", "GPCP" or "TMPA or 3B42" for the abstract, focusing on the period between 2020 and 2024, the period between 2015 and 2019, the period between 2010 and 2014, and the period between 2000 and 2009.

6.2. Data Preprocessing and Statistical Metrics

The validation of SPP or satellite sensor products includes using ground precipitation observations as a reference and mathematical methods (e.g., triple-collocation method and generalized three-cornered hat method) that do not depend on ground data as the benchmark. Most of the SPP validation studies have used the former method. The validation process of the SPE is illustrated in Figure 5. However, obtaining 'true' precipitation data that match the time and space scales of satellite data or possess the same spatial coverage is often challenging. To address this issue, it is common practice to compare SPEs with reference precipitation data, such as ground observations or satellite radar measurements [160], which are considered to have smaller estimation errors. Recognizing the increasing significance of a ground validation network for global precipitation measurements [161], collecting reference precipitation data (from gauges, disdrometers, or radars) serves as the initial step, which is followed by performing spatial and temporal matching tasks. Ultimately, a comparison between the SPE and reference data can be conducted.

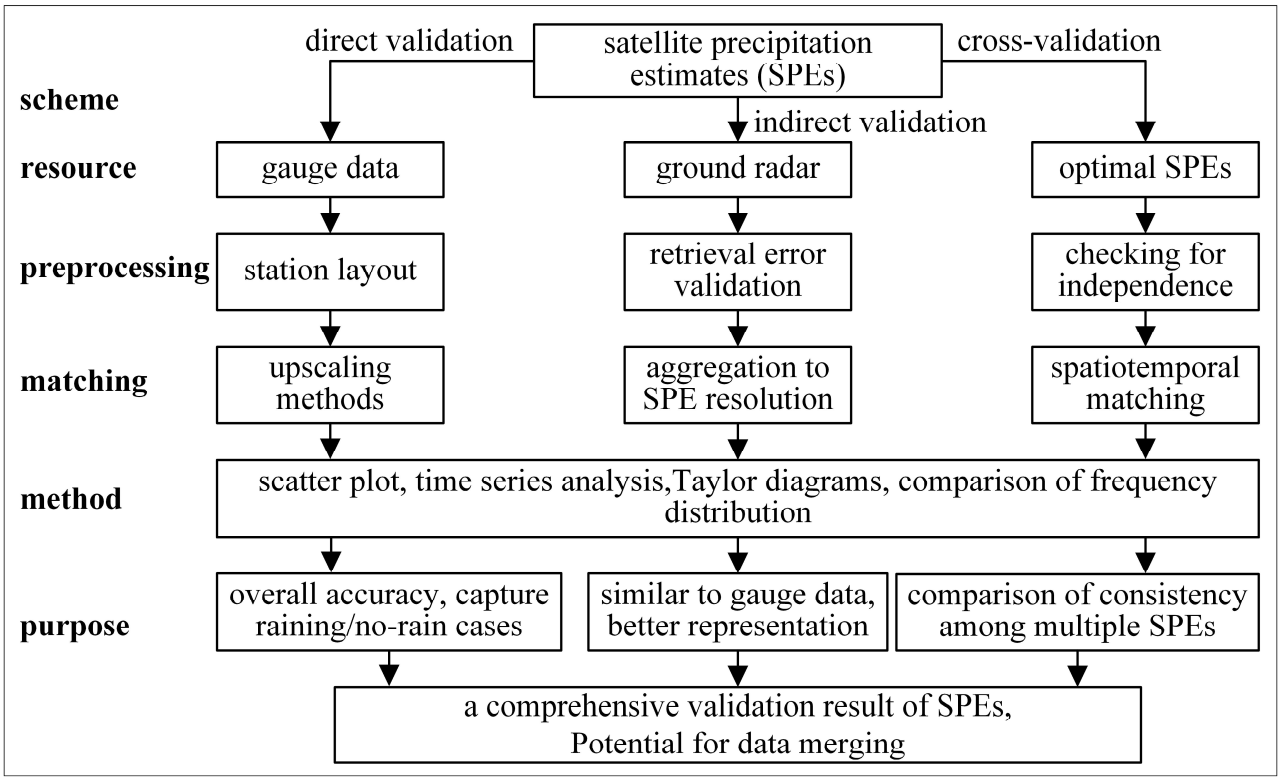

Figure 5. Schematic diagram showing the SPE validation process.

Global validation studies are constrained by temporal and spatial inconsistencies in the reference data [162]. Consequently, numerous studies have been conducted over the past three decades to validate SPEs across different continents and spatiotemporal scales, such as river or lake basins or entire countries [156,157,163–171]. Some of these efforts have focused on analyzing the relationship between SPE performance and season/latitude [155,172], while others have assessed the impact of elevation on SPE performance [173–177]. Additionally, research has explored how precipitation rates influence SPE accuracy and investigated the relationships between precipitation types and SPE performance [171,172,178–181]. Certain studies have also examined extreme precipitation events and tropical cyclones [182–185], compared SPE performance in arid versus wet regions [186,187], or conducted global validations instead of validating a single SPE [53,143,188,189].

After determining the study region and scale, the next step involves comparing SPEs with reference data; this comparison process necessitates spatial and temporal matching.

Point–grid comparisons directly match the pixels and gauge(s) within each dataset [147]. Grid–grid comparisons integrate multiple pixels and gauges within an area into a larger grid scale, followed by matching the resulting grids [190]. These matching processes always involve calculating either arithmetic mean values (e.g., [175]) or weighted values (e.g., using the Thiessen polygon method) of the gauges in each pixel (e.g., [191]). When utilizing radar measurements as references, it is essential to adjust the grids to a consistent scale through spatial matching methods (e.g., interpolation method) [192,193]. The temporal matching process entails aggregating precipitation data to identical timescales, such as from hourly to daily to monthly scales (Figure 5).

Obtaining both quantitative and qualitative accuracy is the ultimate objective of these processes. The most commonly employed approach involves constructing scatter plots to examine the overall performance of statistical prediction equations using validation indices, such as the coefficient of determination (R^2), accuracy (A) (commonly referred to as bias), precision (P), and uncertainty (U) (usually denoted by the root mean square error [RMSE]) [194]. Additionally, categorical metrics including probability of detection (POD), false alarm rate (FAR), and Heidke Skill Score (HSS) [147] are utilized. Furthermore, Taylor diagrams [195], spatiotemporal patterns, and their corresponding D values are frequently adopted for illustrating both the quantitative and qualitative accuracies of SPEs [196]. The D value represents the disparity between the SPE and reference data.

6.3. Uncertainties and Recommendations for SPPs

Despite recent advancements, SPPs are not exempt from uncertainties [171,197–200]. The uncertainties of MPE products primarily stem from the data sources and combining algorithms [201,202]. Evidently, the uncertainties in IR-based and PMW-based estimations propagate to MPEs [203]. For instance, Kirstetter et al. [204] observed significant uncertainties in IR-based precipitation estimates that carried over into the final merged product. Gebregiorgis et al. [205] argued that the improvement relative to the TMPA IR component was more substantial than that relative to the PMW retrieval due to the Kalman smoother and PMW morphing steps in IMERG reducing the reliance on IR compared to TMPA. Studying and quantifying the uncertainties in both IR-based and PMW-based precipitation estimations pose a challenge [81,111]. This becomes even more intricate when examining MPE uncertainties.

Despite the similar input data, there are significant variations in the methods used for estimating precipitation in MPE algorithms through interpolation and merging. The selection of a combining method also introduces considerable uncertainties. Each available combining method has its own advantages and disadvantages (Table 3). Generally, the cloud-motion-based approach heavily relies on PMW data, where PMW estimates are propagated along cloud motions from the observation time to the target analysis time [26,110]. One notable challenge is that these algorithms implicitly assume the linear evolution of precipitation between PMW images over time. Another limitation of this approach is that the cloud tops detected with IR imagery may move at different speeds than the underlying precipitation features. Although this discrepancy can be adjusted using ground radar data, it may not adequately account for precipitation within the moving interval. Most other methods inherently assume that PMW estimates accurately represent instantaneous precipitation rates. The key to this approach lies in the temporally changing and regionally dependent empirical relationship between IR Tb and PMW precipitation intensity. However, a direct physical connection between precipitation and cloud-top temperature is absent, leading to significant errors in IR precipitation estimates and consequently affecting the final merged PMW–IR estimates [25,29]. Furthermore, uncertainties arise in the distribution of precipitation due to the subjective assumptions made for the rain/no-rain threshold. Generally, the performance of these methods heavily relies on the quality of the utilized PMW estimates, while spatial patterns are closely associated with IR data. In order to successfully obtain merged estimates using a weighted-average-based method, accurately defining the bias and error structures

of individual data sources is crucial. Particularly, it is essential to investigate the relationship among errors in various individual data sources.

Table 3. Advantages and limitations of combining methods.

Methodology	Advantages	Limitations	Usage in SPEs
Cloud motion	Assumption: no relation between IR Tb and underlying rainfall	Assumption: precipitation linearly evolves during the time between PMW images; ground rainfall and cloud tops move at different speeds.	IMERG, MORPH, GSMaP
Probability matching	Latency of PMW data less critical; a reasonable measure of cloud movement; Computationally fast	Indirectness of the IR to sense rainfall itself; subjective rain-no-rain threshold	TMPA, AGPI, PERSIANN-CCS, CMORPH-CDR
Adjustment ratio			GPCP
Regression-based			MIRRA; SCaMPR
neural network			PERSIANN, IMERG
Weighted average	Flexible input data	Definitions of the bias and error structures	GPCP, CMAP

To enhance accuracy, MPE algorithms can incorporate ground-based observations [25,111] and integrate different correction procedures. However, these algorithmic variations and the corresponding correction techniques may introduce diverse uncertainties [206]. Furthermore, continuous updates to the algorithms contribute to their evolving nature. Additionally, the spatiotemporal aggregation of precipitation estimates introduces uncertainty, such as inconsistency even after applying normalization processes [97,207]. For instance, the inconsistencies among sensors carried on various satellites (e.g., SSM/I and SSMIS sensors; GOES Imager and ABI sensors) can lead to temporal aggregation uncertainties [29], while the disparities among heterogeneous sensor types (e.g., SSMIS, ATMS, AMSR-E and GMI of PMW sensors; ABI SEVIRI and AHI of GEO-IR sensors) may result in spatial aggregation uncertainties [200,208]. These inconsistencies primarily arise from differences in data quality, sampling scales, sensor frequencies, and blending processes.

Table 4. Examples of SPP evaluation studies.

SPP	Region	Scale	Main Results					Reference	Remarks
3B42 V7 3B42 RT V7	Global	Daily	Bias	U.S.	East Asia	Europe	Australia	[189]	All seasons
			3B42	0.27	−6.96	−6.76	−16.89		
			RT	−12.57	−38.63	−28.09	−41.28		
3B42RT V6 CMORPH V0.x	Australia	Daily		POD	FAR	RMSE/mm		[155]	validation for 5 Jan 2005
			CMORPH	0.55	0.28	7.9			
	Northwestern Europe			POD	FAR	RMSE/mm			validation for 18 Jan 2006
			3B42RT	0.57	0.17	4.4			
GSMaP-MVK V4.8.4 CMORPH V0.x 3B42 V6 PERSIANN	Continental U.S. (CONUS)	Daily	Bias/%	GSMaP	CMORPH	3B42	PERSIANN	[209]	Winter
			West	−50	−75	−41	−27		
			East	−32	−48	−8	−23		
			West	77	88	−8	72		Summer
			East	25	32	−13	28		
CMORPH V0.x PERSIANN 3B42 V6 3B42RT V6	central U. S.	hourly		3B42RT	CMORPH	3B42	PERSIANN	[179]	Except 3B42, all SPPs are unadjusted warm month
			POD	0.41	0.74	0.42	0.55		
			FAR	0.80	0.62	0.83	0.58		
			POD	0.28	0.47	0.22	0.47		
			FAR	0.63	0.46	0.46	0.14		Cold month
			Bias/%	56	50	2	43		All data
3B42 V7 3B42RT V7	CONUS	Daily		Mountainous areas		CONUS		[210]	-
				bias/%	RMSE/mm	bias/%	RMSE/mm		
			3B42	−25.88	0.74	−2.37	0.92		
			3B42RT	−27.97	1.1	0.22	0.75		

Table 4. *Cont.*

SPP	Region	Scale	Main Results				Reference	Remarks
IMERG V03 3B42RT V7	U.S.	Daily	IMERG: 8–30% 3B42RT: 2–18%				[205]	Uncalibrated SPPs
IMERG V06 3B42 V7	U.S., Mexico	Annual	IMERG: −1.25%; 3B42: −7.17%				[184]	all data
		hourly	IMERG: −50.1–54.9%; 3B42: 2.9–56.3% (TCP) (statistically significant differences ($p < 0.05$)					Tropical cyclone precipitation (TCP)
IMERG V05 3B42 V7	China	Annual		bias		RMSE/mm	[183]	Extreme precipitation
			IMERG	−0.07		42.51		
			3B42	−0.07		23.35		
IMERG V06 3B42 V7 CMORPH V1.0 GSMaP-gauge V6/V7 PERSIANN-CDR	China	Daily	IMERG: ~5% (−5–10%); 3B42: ~5% (−5–10%) CMORPH: ~−5% (−10–5%) GSMaP: ~−5% (−10–1%) CDR: ~8% (−5–15%)				[168]	The 25th and 75th percentiles
3B42RT V7 PERSIANN-CCS CMOROH	Iran	6-Hourly		bias/%	POD	FAR	[211]	3B42RT V7 PERSIANN-CCS are near real-time, and CMOROH is after real time
			3B42RT	−56.06	0.05	0.89		
			PERSIANN	144.08	0.36	0.13		
			CMOROH	−8.01	0.44	0.91		
		Daily Monthly Annual	bias/%	Daily	Monthly	Annual		
			3B42RT	−56.12	−56.13	−56.14		
			PERSIANN	143.86	143.84	143.84		
			CMOROH	−8.08	−8.10	−8.10		

Table 4. *Cont.*

SPP	Region	Scale	Main Results	Reference	Remarks
3B42 V7 3B42RT V7 CMORPH-RAW V1.0 CMORPH V1.0 GSMaP-MVK V6 GSMaP-gauge V6 PERSIANN-RAW PERSIANN-CDR	Central Asia	Daily	3B42RT/3B42/CMORPH-RAW/CMORPH: POD < 30%, miss 70%; GSMaP_Gauge: POD > 60%; FAR < 30%; PERSIANN-CDR: POD > 60%, FAR > 40%	[212]	Winter
			all SPPs: the worst performance, POD < 30%, highest misses, FAR > 60% CMORPH_RAW, CMORPH:_miss up to 100%		Over the desert region in summer
CMORPH V0.x 3B42 V6 3B42RT V6	Mountainous	Monthly	3B42: −14%; 3B42RT: 13%; CMORPH: 11%	[213]	
	Highlands of Columbia	Monthly	3B42: −16%; 3B42RT: −17%; CMORPH: −9%		
IMERG CMORPH-RAW V1.0 GSMAP_NRT V6 PERSIANN-CDR-gauge	Africa	Daily	RMSE/mm IMERG: 0.6–4.1; CMORPH: 0.9–5.0 GSMAP: 0.8–4.5; PERSIANN: 0.7–5.2 Corrected satellite products depict notable agreement for POD and FAR	[171]	Heavy precipitation monitoring: all IMERG, uncorrected PERSIAN_CDR and GSMAP_NRT Flood monitoring: CMORPH and PERSIANN-CDR.
3B43 V6 3B42 V6 CMAP V1.2 GPCP V2 GPCP 1DD CMORPH V0.x	Complex topography, East Africa	Monthly	GPCP: 20%; CMAP: 9% 3B43: 8%	[173]	Data pairs = 168
			1DD: 23%; 3B42: 6%; CMORPH: 2%		Data pairs = 306
3B42RT V6 CMORPH V0.x PERSIANN	Ethiopian river basins	Monthly	CMORPH: 11%; 3B42RT: 5%; PERSIANN: −43%	[175]	
CMORPH V1.0 3B42RT V7 3B42 V7	Southern South America	Daily	3B42: −30–32%; 3B42RT: −60–60% CMORPH: −73–81%	[214]	

Quantifying SPE errors is an immensely challenging task due to their association with a multitude of factors, particularly at fine spatiotemporal resolutions. The anticipated performance of SPEs may be hindered by various common underlying factors, climatic and meteorological conditions, seasonal variations, precipitation intensities, and latitudes. Consequently, it is not possible to designate any single algorithm or SPP as superior to the others (Table 4). The abovementioned validation practices yield consistent conclusions: MPEs face difficulties in accurately estimating light precipitation rates, snowfall, and orographic rain. SPPs exhibit substantial uncertainties in regions at moderate to high latitudes, especially during cold seasons and over areas characterized by complex terrain. For instance, Tian et al. [215] and Tian and Peters-Lidard [188] investigated the errors of HRPPs (GSMaP-MVK, CMORPH, 3B42, and PERSIANN) worldwide and reported that while SPPs perform well for precipitation rates exceeding 40 mm/d, they tend to underestimate a significant portion of light precipitation (<10 mm/d) up to approximately 40%. In addition, significant uncertainties (ranging from 100% to 140%) were observed over high latitudes (poleward of 40° latitude), particularly during the cold season, as well as in regions characterized by complex terrain (such as the Tibetan Plateau), coastlines, and water bodies. Yong et al. [189] reported that the overall bias of 3B42 falls within the range of −16.89% to 0.27% (RMSE: 5.28–8.52 mm/d), while indicating that, globally, precipitation is overestimated by 12.57–41.28% with respect to 3B42RT (RMSE: 5.07–7.53 mm/d). Tang et al. [168] demonstrated that HRPPs' overall biases on a daily scale in China are within ±10%, including IMERG, 3B42, CMORPH, GSMaP-gauge and PERSIANN-CDR. The results of IMERG validation studies, as summarized by Pradhan et al. [58], confirm that the bias of IMERG ranges from −58.77% to 13.5% (9.7–47.5 mm/h) for extreme events and from −28.7% to 41.4% on the daily scale in hydrological applications. These previous studies indicate that the latest IMERG product exhibits significant improvement over the TRMM dataset, highlighting its potential for various present and future applications.

Previous studies primarily focused on PMW sensor estimates instead of SPPs. For instance, Zhu et al. [216] indicated that PMW imagers are superior to sounders and morph (PMW-IR using the morphing technique). Among the other imagers, TMI shows the best performance with a bias of −8.8%, while SSMIS shows the worst performance with a bias of 39.8%. GMI is skillful in detecting heavy rains but overestimates light to moderate rains. All sounders along with morph have large biases, typically >120%. The advantages of PMW imagers over sounders were mentioned by Chen et al. [217]. They also revealed the inefficiency of GMI in winter/spring and over arid/semi-arid regions. Sui et al. [218] reported the best performance of MHS among other sensors including GMI, SSMIS, ATMS, AMSR-2 and SAPHIR.

Land cover also matters. Generally, large uncertainties are observed over low-lying, urban, water, and coastal areas. In addition, Li et al. [219] analyzed the performance of PMW sensor estimates for quantifying extreme rates. The results showed that MHS is the best sensor in this regard, while SAPHIR shows the worst performance.

7. Conclusions and Outlook

The precipitation community has greatly benefited from the availability of multiple long-term satellite precipitation records derived from both infrared (IR) and passive microwave (PMW) sensors. Remarkable advancements have been achieved in the development of multi-sensor precipitation estimation (MPE) over the past two to three decades. Currently, MPE stands as the predominant method for generating global satellite precipitation products (SPPs). Satellites and sensors, particularly those within the Global Precipitation Measurement (GPM) constellation, offer invaluable data support. The key to obtaining accurate MPEs lies in leveraging PMW- and IR-based observations and/or precipitation estimates through a combination of methods. These estimates are crucial for advancing MPE techniques, while other sources such as radar measurements, ground observations, and additional precipitation datasets play complementary roles.

Two broad categories of techniques have been developed for integrating PMW precipitation and/or IR observations. The first category, known as the cloud-motion-based approaches (employed in CMORPH, GSMaP, and GPM IMERG), involves propagating and interpolating instantaneous PMW estimates using the cloud motion vectors derived from IR images. The second category primarily encompasses approaches based on PMM, AR, regression, and NN methods. These approaches inherently assume that PMW estimates represent accurate measurements of instantaneous precipitation rates (as seen in TMPA, PERSIANN, and GPCP). Additionally, a weighted-average-based method is utilized in the GPCP and CMAP products. Numerous international projects, programs, and research studies have investigated MPE uncertainties with a primary focus on SPP performance evaluation while gradually establishing validation methodologies. Generally speaking, MPE uncertainties arise due to data quality issues (primarily related to PMW and IR estimates) as well as the MPE algorithms themselves. Despite significant advancements in MPE techniques over time [16], several challenges still remain at the forefront [58,220]. Future attention should be directed toward addressing these issues.

(1) Improved PMW sensors are crucial for the advancement of MPE, and the current GPM constellation has greatly contributed to this field over the past few decades. It has been observed that the performance of almost all SPEs in MPE heavily relies on the accuracy of PMW estimates [55,199]. However, due to the limited spatial and temporal resolution of LEO sensors, the present PMW data are collected at a spatial resolution of approximately 0.1° every three hours, leading to deficiencies in recovering precipitation at the sub-mesoscale.

(2) The improved consistency among multi-sensor data and the optimal integration of multi-sensor retrievals are essential. Inconsistencies arise from the distinct spatiotemporal samplings and error structures inherent in the different instruments and frequency channels [30]. Coupled with diverse estimation algorithms, these characteristics contribute to uncertainties in precipitation retrievals [43,221]. Despite the existence of various proposed and developed algorithms, determining the optimal integration of multi-sensor estimates has remained a focal point in MPE studies, which continues to be an ongoing endeavor.

(3) Emphasis should be placed on estimations of extremely low and high precipitation, hail, and snowfall, as well as precipitation over water bodies, mountainous regions, and coastal areas. The challenge in estimating orographic precipitation primarily stems from difficulties in detecting the influence of topography on precipitation [96,217]. Numerous studies have confirmed the inadequate performance of statistical postprocessing (SPP) methods at high latitudes (above 40° latitude), particularly during the cold season, and over regions with complex terrain such as the Tibetan Plateau, coastlines, and water bodies [155,217]. SPPs also exhibit significant uncertainties when representing light and extreme precipitation events, hailstorms, and snowfall [168,188,222]. Therefore, addressing these issues is imperative for enhancing global statistical postprocessing efforts.

(4) The characterization and quantification of retrieval uncertainties at multiple scales should be enhanced. It has been confirmed that the performance of these precipitation estimates is influenced by underlying factors, climatic conditions, meteorological conditions, seasons, precipitation intensities, and latitudes [155,168,171]. Furthermore, these estimates are derived at various resolutions, and their performance is associated with spatiotemporal scales [191,223]. Numerous evaluation studies have been conducted on this subject; however, further research is required to generalize retrieval uncertainties under diverse environmental conditions. Quantitative evaluations are expected to yield more significant results when synthesizing precipitation estimates across a wide range of environmental conditions while considering multiple factors at various scales.

The GPM constellation continues to play a crucial role in supporting MPE. Notably, recent advancements in satellite systems and sensors have been made during the preparation of this paper, which hold great potential for enhancing precipitation retrievals. These include the Weather System Follow-on–Microwave (WSF-M) satellite system (launched in April 2024), as well as the Earth Clouds, Aerosol, and Radiation Explorer (EarthCare)

satellite equipped with Atmospheric Lidar (ATLID) and Cloud Profiling Radar (CPR) instruments (launched in May 2024) by ESA and JAXA. Additionally, upcoming satellite systems and sensors are being planned to enhance the MPE observational capability. These include the Microwave Imager (MWI) on the Meteorological Operational-Second Generation (METOP-SG) B-series, scheduled for 2025 by ESA and EUMETSAT, as well as the ATMS on JPSS-3, planned for January 2026 by NOAA and NASA. The future utilization of infrared sensors and lightning sensors on geostationary satellites will be emphasized, such as the Meteosat Third-Generation (MTG) Imaging mission satellite-2 (MTG-I 2), expected in 2026, and MTG-Sounding 1 (MTG-S 2), anticipated in 2025 by EUMETSAT and ESA. In addition, the FY-3G satellite, China's first precipitation measurement satellite, was launched on April in 2023. It was deployed with a precipitation measurement radar (PMR) and the Microwave Radiation Imager-Rainfall Mission (MWRI-RM) [224]. It has precipitation detection capabilities comparable to the current GPMCO. It aims to accurately measure the occurrence, type, and intensity of any precipitation around the world, including over oceans and complex terrain.

Many international group or projects, such as GPCP, AIP, PIP and PEHRPP, had given impetus to MPE and SPE progress. IPWG has been providing a forum to exchange information on methods for measuring precipitation and the impact of spaceborne precipitation measurements for 20 years. GPM has been tracking rain and snow around the globe for over 10 years. These existing international groups or missions or project like IPWG and GPM will continue their support of MPE.

Author Contributions: Conceptualization, R.G., X.F. and Y.L.; writing—original draft preparation, R.G.; writing—review and editing, X.F., Y.L. and H.Z.; visualization, R.G. and X.F.; supervision, Y.L. and X.F.; funding acquisition, R.G. All authors have read and agreed to the published version of the manuscript.

Funding: This research was funded by the First Class Discipline Research Special Project under Education Department of Inner Mongolia Autonomous Region, grant number YLXKZX-NSD-041; the National Natural Science Foundation of China, grant number 41901051,; the Natural Science Foundation of Inner Mongolia, grant number 2021LHMS04006; High-level talent research start-up fund project, grant number 2020YJRC008; and the National Natural Science Foundation of China, grant number 41961058.

Acknowledgments: The authors would like to thank Chris Kidd at the University of Maryland for his comments and guidance.

Conflicts of Interest: The authors declare no conflicts of interest.

Relevant Abbreviations and Definitions of Satellites, Sensors, and Agencies

Abbreviation	Definition
AMSR	Advanced Microwave Scanning Radiometer
AMSU-B	Advanced Microwave Sounding Unit-B
ATLID	Atmospheric Lidar
ATMS	Advanced Technology Microwave Sounder
BoM	Bureau of Meteorology
CEOS	Committee on Earth Observation Satellites
CGMS	Coordination Group for Meteorological Satellites
CMA	China Meteorological Administration
CPC	Climate Prediction Center
CPR	Cloud Profiling Radar
DMSP	Defense Meteorological Satellite Program
DOD	U.S. Department of Defense
DPR	Dual Frequency Precipitation Radar

Abbreviation	Definition
DWD	German Weather Service (Deutscher Wetterdienst)
EarthCare	Earth Clouds, Aerosol and Radiation Explorer
EOSSDIS	Earth Observing System Science and Data Information System
ESA	European Space Agency
EUMETSAT	European Organisation for the Exploitation of Meteorological Satellites
FY	FengYun
GCOM-W	Global Change Observation Mission for Water
GEO	Geostationary
GMI	GPM Microwave Imager
GEWEX	Global Energy and Water Cycle Experiment
GMS	Geostationary Meteorological Satellite
GOES	Geostationary Operational Environmental Satellite
GOS	Global Observing System
GV	Ground validation
IPWG	International Precipitation Working Group
JAXA	Japan Aerospace Exploration Agency
JCAB	Japanese Ministry of Transport Civil Aviation Bureau
JMA	Japan Meteorological Agency
JPSS	Joint Polar Satellite System
LEO	Low-Earth orbit
Meteosats	Meteorological satellites
METOP	Meteorological operational satellite
MHS	Microwave Humidity Sounder
MTG	Meteosat Third-Generation
MTSAT	Multifunctional Transport Satellites series
MWI	Microwave Imager
MWRI-RM	Microwave Radiation Imager-Rainfall Mission
NASA	National Aeronautics and Space Administration
NASDA	Japan's National Space Development Agency
NCEI	National Centers for Environmental Information
NEXRAD	Next-Generation Weather Radar
NOAA	National Oceanic and Atmospheric Administration
NRSCC	National Remote Sensing Center of China
OPERA	Operational Programme for the Exchange of Weather Radar Information in Europe
PMR	Precipitation Measurement Radar
PPS	Precipitation Process System
PR	Precipitation Radar
P-VC	Precipitation Virtual Constellation
SAPHIR	Sonder Atmospherique du Profil d'Humidite Intertropicale par Radiometrie
SMS	Synchronous Meteorological Satellites
S-NPP	Suomi National Polar-orbiting Partnership
SSM/I	Special Sensor Microwave Imager
SSMIS	Special Sensor Microwave Imager-Sounder
TMI	TRMM Microwave Imager
TRMM	Tropical Rainfall Measurement Mission
UDEL	University of Delaware
WCRP	World Climate Research Programme
WSF-M	Weather System Follow-on–Microwave
WMO	World Meteorological Organization

Relevant Abbreviations and Definitions of Algorithms, Products, and Systems

Abbreviation	Definition
AGPI	adjusted GOES precipitation index
AMW	Active Microwave

Abbreviation	Definition
CDR	Climate Data Record
CMAP	Climate Prediction Center Merged Analysis of Precipitation
CMORPH	Climate Prediction Center Morphing method
CRU	Climatic Research Unit
GHCN	Global Historical Climatology Network
GPCC	Global Precipitation Climatology Centre
GPCP	Global Precipitation Climatology Project
GPI	Global Precipitation Index
GPM	Global Precipitation Measurement
GSMaP	Global Satellite Mapping of Precipitation
HRPPs	High Resolution Precipitation Products
IMERG	Integrated Multi-satellite Retrievals for GPM
IR	Infrared
MPE	Multi-sensor precipitation estimation
MW	Microwave
NEXRAD	Next-Generation Weather Radar
OPI	Outgoing Long-wave Radiation Precipitation Index
PERSIANN CCS	PERSIANN Cloud Classification System
PMW	Passive microwave
PREC	Precipitation Reconstruction
SPE	Satellite precipitation estimation
SPP	Satellite precipitation product
Tb	Brightness temperature
TMPA	TRMM Multi-Satellite Precipitation
UDEL	University of Delaware
USHCN	U.S. Historical Climatology Network
VIS/IR	Visible/infrared

References

1. Barrett, E.C.; Martin, D.W. *The Use of Satellite Data in Rainfall Monitoring*, 1st ed.; Academic Press: London, France, 1981; p. 340.
2. Tobler, W. On the first law of geography: A reply. *Ann. Assoc. Am. Geog.* **2004**, *94*, 304–310. [CrossRef]
3. Shepherd, J.M.; Burian, S.; Liu, C.; Bernardes, S. Satellite Precipitation Metrics to Study the Energy-Water-Food Nexus Within the Backdrop of an Urbanized Globe. Earthzine. Available online: https://earthzine.org/satellite-precipitation-metrics-to-study-the-energy-water-food-nexus-within-the-backdrop-of-an-urbanized-globe/ (accessed on 1 December 2024).
4. Trenberth, K.E.; Dai, A.; Rasmussen, R.M.; Parsons, D.B. The changing character of precipitation. *Bull. Am. Meteorol. Soc.* **2003**, *84*, 1205–1217. [CrossRef]
5. Kidd, C.; Becker, A.; Huffman, G.J.; Muller, C.L.; Joe, P.; Skofronick-Jackson, G.; Kirschbaum, D.B. So, how much of the Earth's surface is covered by rain gauges? *Bull. Am. Meteorol. Soc.* **2017**, *98*, 69–78. [CrossRef] [PubMed]
6. Trenberth, K.E.; Zhang, Y. How often does it really rain? *Bull. Am. Meteorol. Soc.* **2018**, *99*, 289–298. [CrossRef]
7. Flossmann, A.I.; Manton, M.; Abshaev, A.; Bruintjes, R.; Murakami, M.; Prabhakaran, T.; Yao, Z. Review of Advances in Precipitation Enhancement Research. *Bull. Am. Meteorol. Soc.* **2019**, *100*, 1465–1480. [CrossRef]
8. Barrett, E.C.; Beaumont, M.J. Satellite rainfall monitoring: An overview. *Remote Sens. Rev.* **1994**, *11*, 23–48. [CrossRef]
9. New, M.; Todd, M.; Hulme, M.; Jones, P. Precipitation measurements and trends in the twentieth century. *Int. J. Climatol.* **2001**, *21*, 1889–1922. [CrossRef]
10. Saltikoff, E.; Friedrich, K.; Soderholm, J.; Lengfeld, K.; Nelson, B.; Becker, A.; Tassone, C. An overview of using weather radar for climatological studies: Successes, challenges, and potential. *Bull. Am. Meteorol. Soc.* **2019**, *100*, 1739–1752. [CrossRef]
11. Krajewski, W.F.; Smith, J.A. Radar hydrology: Rainfall estimation. *Adv. Water Resour.* **2002**, *25*, 1387–1394. [CrossRef]
12. Smith, J.A.; Seo, D.J.; Baeck, M.L.; Hudlow, M.D. An intercomparison study of NEXRAD precipitation estimates. *Water Resour. Res.* **1996**, *32*, 2035–2045. [CrossRef]
13. Young, C.B.; Nelson, B.R.; Bradley, A.A.; Smith, J.A.; Peters-Lidard, C.D.; Kruger, A.; Baeck, M.L. An evaluation of NEXRAD precipitation estimates in complex terrain. *J. Geophys. Res.* **1999**, *104*, 19691–19703. [CrossRef]
14. Young, C.B.; Bradley, A.A.; Krajewski, W.F.; Kruger, A.; Morrissey, M.L. Evaluating NEXRAD multisensor precipitation estimates for operational hydrologic forecasting. *J. Hydrometeorol.* **2000**, *1*, 241–254. [CrossRef]
15. Kucera, P.A.; Ebert, E.E.; Turk, J.F.; Levizzani, V.; Kirschbaum, D.; Tapiador, F.J.; Loew, A.; Borsche, M. Precipitation from space: Advancing Earth system science. *Bull. Am. Meteorol. Soc.* **2013**, *94*, 365–375. [CrossRef]
16. Levizzani, V.; Kidd, C.; Kirschbaum, D.B.; Kummero, C.D.; Nakamura, K.; Turk, F.J. *Satellite Precipitation Measurement*, 1st ed.; Springer: Berlin/Heidelberg, Germany, 2020. [CrossRef]

17. Kidd, C.; Kniveton, D.R.; Todd, M.C.; Bellerby, T.J. Satellite rainfall estimation using combined passive microwave and infrared algorithms. *J. Hydrometeorol.* **2003**, *4*, 1088–1104. [CrossRef]
18. Ferraro, R.R. Past, present and future of microwave operational rainfall algorithms. In *Measuring Precipitation From Space: EURAINSAT and the Future*, 1st ed.; Levizzani, V., Bauer, P., Eds.; Springer: Dordrecht, The Netherlands, 2007; pp. 189–198. [CrossRef]
19. Kozu, T.; Kawanishi, T.; Kuroiwa, H.; Kojima, M.; Oikawa, K.; Kumagai, H.; Okamoto, K.; Okumura, M.; Nakatsuka, H.; Nishikawa, K.K. Development of Precipitation Radar onboard the Tropical Rainfall Measuring Mission satellite. *IEEE Geosci. Remote Sens. Lett.* **2001**, *39*, 102–116. [CrossRef]
20. Hou, A.Y.; Kakar, R.K.; Neeck, S.; Azarbarzin, A.A.; Kummerow, C.D.; Kojima, M.; Oki, R.; Nakamura, K.; Ighchi, T. The Global Precipitation Measurement mission. *Bull. Am. Meteorol. Soc.* **2014**, *95*, 701–722. [CrossRef]
21. Skofronick-Jackson, G.; Petersen, W.A.; Berg, W.; Kidd, C.; Stocker, E.F.; Kirschbaum, D.B.; Kakar, R.; Braun, S.A.; Huffman, G.J.; Iguchi, T.; et al. The Global Precipitation Measurement (GPM) mission for science and society. *Bull. Am. Meteorol. Soc.* **2017**, *98*, 1679–1695. [CrossRef] [PubMed]
22. Ebert, E.E.; Manton, M.J.; Arkin, P.A.; Allam, R.J.; Holpin, G.E.; Gruber, A. Results from the GPCP algorithm intercomparison programme. *Bull. Am. Meteorol. Soc.* **1996**, *77*, 2875–2888. [CrossRef]
23. Ebert, E.E.; Manton, M.J. Performance of satellite rainfall estimation algorithms during TOGA COARE. *J. Atmos. Sci.* **1998**, *55*, 1537–1557. [CrossRef]
24. Turk, F.J.; Ebert, E.E.; Oh, H.J.; Sohn, B.J.; Levizzani, V.; Smith, E.A.; Ferraro, R. Validation of an operational global precipitation analysis at short time scales. In Proceedings of the 12th Conference on Satellite Meteorology and Oceanography, Long Beach, CA, USA, 8–13 February 2003. Available online: https://ams.confex.com/ams/pdfpapers/56865.pdf (accessed on 1 December 2024).
25. Huffman, G.J.; Adler, R.F.; Bolvin, D.T.; Gu, G.; Nelkin, E.J.; Bowman, K.P.; Hong, Y.; Stocker, E.F.; Wolff, D.B. The TRMM multisatellite precipitation analysis (TMPA): Quasi-global, multiyear, combined-sensor precipitation estimates at fine scales. *J. Hydrometeorol.* **2007**, *8*, 38–55. [CrossRef]
26. Joyce, R.J.; Janowiak, J.E.; Arkin, P.A.; Xie, P. CMORPH: A method that produces global precipitation estimates from passive microwave and infrared data at high spatial and temporal resolution. *J. Hydrometeorol.* **2004**, *5*, 487–503. [CrossRef]
27. Kubota, T.; Shige, S.; Hashizume, H.; Aonashi, K.; Takahashi, N.; Seto, S.; Hirose, M.; Takayabu, Y.N.; Ushio, T.; Nakagawa, K.; et al. Global Precipitation Map Using Satellite-Borne Microwave Radiometers by the GSMaP Project: Production and Validation. *IEEE Trans. Geosci. Remote* **2007**, *45*, 2259–2275. [CrossRef]
28. Hsu, K.L.; Gao, X.; Sorooshian, S.; Gupta, H.V. Precipitation estimation from remotely sensed information using artificial neural networks. *J. Appl. Meteorol.* **1997**, *36*, 1176–1190. [CrossRef]
29. Hong, Y. Precipitation Estimation from Remotely Sensed Information Using Artificial Neural Network-Cloud Classification System. Ph.D. Thesis, The University of Arizona, Tucson, AZ, USA, 2003. UMI Number 3108912. Available online: https://www.proquest.com/openview/d8936b9522c229acd98f158e15aa7755/1?pq-origsite=gscholar&cbl=18750&diss=y (accessed on 1 December 2024).
30. Huffman, G.J.; Bolvin, D.T.; Braithwaite, D.; Hsu, K.; Joyce, R.; Kidd, C.; Nelkin, E.J.; Sorooshian, S.; Tan, J.; Xie, P. NASA Global Precipitation Measurement (GPM) Integrated Multi-satellite Retrievals for GPM (IMERG). In *Algorithm Theoretical Basis Document (ATBD)*; NASA/GSFC: Greenbelt, MD, USA, 2018. Available online: https://gpm.nasa.gov/sites/default/files/document_files/IMERG_ATBD_V5.2_0.pdf (accessed on 1 December 2024).
31. D'souza, G.; Barrett, E.C.; Power, C.H. Satellite rainfall estimation techniques using visible and infrared imagery. *Remote Sens. Rev.* **1990**, *4*, 379–414. [CrossRef]
32. Kidd, C.; Barrett, E.C. The use of passive microwave imagery in rainfall monitoring. *Remote Sens. Rev.* **1990**, *4*, 415–450. [CrossRef]
33. Wilheit, T.; Adler, R.; Avery, S.; Barrett, E.; Bauer, P.; Berg, W.; Chang, A.; Ferriday, J.; Grody, N.; Goodman, S.; et al. Algorithms for the retrieval of rainfall from passive microwave measurements. *Remote Sens. Rev.* **1994**, *11*, 163–194. [CrossRef]
34. Arkin, P.A.; Ardanuy, P.E. Estimating climatic-scale precipitation from space: A review. *J. Clim.* **1989**, *2*, 1229–1238. [CrossRef]
35. Barrett, E.C. Satellite rainfall monitoring for agrometeorology: Operational problems, practices and prospects. *EARSeL Adv. Remote Sens.* **1993**, *2*, 66–72. Available online: https://earsel.org/wp-content/uploads/2016/11/2-2_09_Barrett.pdf (accessed on 1 December 2024).
36. Petty, G.W. The status of satellite-based rainfall estimation over land. *Remote Sens. Environ.* **1995**, *51*, 125–137. [CrossRef]
37. Petty, G.W.; Krajewski, W.F. Satellite estimation of precipitation over land. *Hydrol. Sci. J.* **1996**, *41*, 433–451. [CrossRef]
38. Levizzani, V. Satellite rainfall estimates: A look back and a perspective. In Proceedings of the 2000 EUMETSAT Meteorological Satellite Data User's Conference, Bologna, Italy, 29 May–2 June 2000; pp. 344–353. Available online: https://www.researchgate.net/publication/257114602_Satellite_rainfall_estimates_a_look_back_and_a_perspective (accessed on 1 December 2024).
39. Kidd, C. Satellite rainfall climatology: A review. *Int. J. Climatol.* **2001**, *21*, 1041–1066. [CrossRef]
40. Levizzani, V.; Amorati, R.; Meneguzzo, F. A review of satellite-based rainfall estimation methods. In *Multiple-Sensor Precipitation Measurements, Integration, Calibration and Flood Forecasting*; European Commission Project MUSIC Report (EVK1-CT-2000-00058); 2002; Volume 66. Available online: https://www.academia.edu/download/45755676/A_Review_of_Satellite-based_Rainfall_Est20160518-31135-5xarl.pdf (accessed on 1 October 2022).
41. Scofield, R.A.; Kuligowski, R.J. Status and outlook of operational satellite precipitation algorithms for extreme precipitation events. *Weather Forecast.* **2003**, *18*, 1037–1051. [CrossRef]

42. Anagnostou, E.N. Overview of overland satellite rainfall estimation for hydro-meteorological applications. *Surv. Geophys.* **2004**, *25*, 511–537. [CrossRef]
43. Stephens, G.L.; Kummerow, C.D. The remote sensing of clouds and precipitation from space: A review. *J. Atmos. Sci.* **2007**, *64*, 3742–3765. [CrossRef]
44. Michaelides, S.; Levizzani, V.; Anagnostou, E.; Bauer, P.; Kasparis, T.; Lane, J.E. Precipitation: Measurement, remote sensing, climatology and modeling. *Atmos. Res.* **2009**, *94*, 512–533. [CrossRef]
45. Kidd, C.; Levizzani, V.; Turk, J.; Ferraro, R. Satellite Precipitation Measurements for Water Resource Monitoring. *J. Am. Water Resour. Assoc.* **2009**, *45*, 567–579. [CrossRef]
46. Kidd, C.; Levizzani, V.; Laviola, S. Quantitative precipitation estimation from Earth observation satellites, in Rainfall: State of the Science. *Am. Geophys. Union* **2010**, *191*, 127–158. [CrossRef]
47. Durkee, J. Precipitation measurement and the advancement toward global observations. *Geogr. Compass* **2010**, *4*, 956–978. [CrossRef]
48. Prigent, C. Precipitation retrieval from space: An overview. *C. R. Geosci.* **2010**, *342*, 380–389. [CrossRef]
49. Kidd, C.; Levizzani, V. Status of satellite precipitation retrievals. *Hydrol. Earth Syst. Sci.* **2011**, *15*, 1109–1116. [CrossRef]
50. Tapiador, F.J.; Turk, F.J.; Petersen, W.; Hou, A.Y.; García-Ortega, E.; Machado, L.A.T.; Angelis, C.F.; Salio, P.; Kidd, C.; Huffman, G.J.; et al. Global precipitation measurement: Methods, datasets and applications. *Atmos. Res.* **2012**, *104–105*, 70–97. [CrossRef]
51. Hong, Y.; Tang, G.; Ma, Y.; Huang, Q.; Han, Z.; Zeng, Z.; Yang, Y.; Wang, C.; Guo, X. Remote sensing precipitation: Sensors, retrievals, validations, and applications. In *Observation and Measurement of Ecohydrological Processes*, 1st ed.; Li, X., Vereecken, H., Eds.; Springer: Berlin/Heidelberg, Germany, 2019; pp. 107–128. [CrossRef]
52. Knapp, K.R.; Ansari, S.; Bain, C.L.; Bourassa, M.A.; Dickinson, M.J.; Funk, C.; Helms, C.D.; Hennon, C.C.; Holmes, C.D.; Huffman, G.J.; et al. Globally Gridded Satellite Observations for Climate Studies. *Bull. Am. Meteorol. Soc.* **2011**, *92*, 893–907. [CrossRef]
53. Sun, Q.H.; Miao, C.Y.; Duan, Q.Y.; Ashouri, H.; Sorooshian, S.; Hsu, K. A review of global precipitation data sets: Data sources, estimation, and intercomparisons. *Rev. Geophys.* **2018**, *56*, 79–107. [CrossRef]
54. Roca, R.; Alexander, L.V.; Potter, G.; Bador, M.; Jucá, R.; Contractor, S.; Bosilovich, M.G.; Cloché, S. FROGS: A daily $1^\circ \times 1^\circ$ gridded precipitation database of rain gauge, satellite and reanalysis products. *Hydrol. Earth. Syst. Sci. Data* **2019**, *11*, 1017–1035. [CrossRef]
55. Turk, F.J.; Arkin, P.; Ebert, E.E.; Sapiano, M.R. Evaluating high-resolution precipitation products. *Bull. Am. Meteorol. Soc.* **2008**, *89*, 1911–1916. [CrossRef]
56. Maggioni, V.; Meyers, P.C.; Robinson, M.D. A review of merged high-resolution satellite precipitation product accuracy during the Tropical Rainfall Measuring Mission (TRMM) Era. *J. Hydrometeorol.* **2016**, *17*, 1101–1117. [CrossRef]
57. Roca, R.; Haddad, Z.S.; Akimoto, F.F.; Alexander, L.; Behrangi, A.; Huffman, G.J.; Kato, S.; Kidd, C.; Kirstetter, P.E.; Kubota, T.; et al. *The Joint IPWG/GEWEX Precipitation Assessment*; World Climate Research Programme (WCRP): Geneva, Switzerland, 2021; 125p. [CrossRef]
58. Pradhan, R.K.; Markonis, Y.; Godoy, M.R.V.; Villalba-Pradas, A.; Andreadis, K.M.; Nikolopoulos, E.I.; Papalexiou, S.M.; Rahim, A.; Tapiador, F.J.; Hanel, M. Review of GPM IMERG performance: A global perspective. *Remote Sens. Environ.* **2022**, *268*, 112754. [CrossRef]
59. Fischer, F.K.; Winterrath, T. Precipitation measurement techniques, typical data sets, and their application in erosion research and extreme value statistics. In *Precipitation*, 1st ed.; Comino, J.R., Ed.; Elsevier: Amsterdam, The Netherlands, 2021; pp. 147–172. [CrossRef]
60. Levizzani, V.; Gruber, A. The 1st International Precipitation Working Group (IPWG) Workshop. In Proceedings of the 1st IPWG Workshop, Madrid, Spain, 23–27 September 2003; EUMETSAT EUM P34; pp. VII–VIII; ISBN 92-9110-045-5.
61. Turk, J.; Bauer, P. The international precipitation working group and its role in the improvement of quantitative precipitation measurements. *Bull. Am. Meteorol. Soc.* **2006**, *87*, 643–648. [CrossRef]
62. Smith, E.A.; Asrar, G.; Furuhama, Y.; Ginati, A.; Mugnai, A.; Nakamura, K.; Adler, R.F.; Chou, M.D.; Desbois, M.; During, J.F.; et al. International global precipitation measurement (GPM) program and mission: An overview. In *Measuring Precipitation From Space: EURAINSAT and the Future*, 1st ed.; Levizzani, V., Bauer, P., Eds.; Springer: Dordrecht, The Netherlands, 2007; pp. 611–653. [CrossRef]
63. Kidd, C.; Ferraro, R.; Levizzani, V. The Fourth International Precipitation Working Group Workshop. *Bull. Am. Meteorol. Soc.* **2010**, *91*, 1095–1099. [CrossRef]
64. Huffman, G.J.; Klepp, C. Meeting Summary: Fifth workshop of the International Precipitation Working Group. *Bull. Am. Meteorol. Soc.* **2011**, *92*, ES54–ES57. [CrossRef]
65. Levizzani, V.; Kidd, C.; Aonashi, K.; Bennartz, R.; Ferraro, R.R.; Huffman, G.J.; Roca, R.; Turk, F.J.; Wang, N.Y. The activities of the International Precipitation Working Group. *Q. J. R. Meteorol. Soc.* **2018**, *144*, 3–15. [CrossRef]
66. Levizzani, V.; Bauer, P.; Turk, F.J. *Satellite Precipitation Measurement*, 1st ed.; Springer: Berlin/Heidelberg, Germany, 2007.
67. Islam, T.; Hu, Y.; Kokhanovsky, A.; Wang, J. *Remote Sensing of Aerosols, Clouds, and Precipitation*, 1st ed.; Elsevier: Amsterdam, The Netherlands, 2017.
68. Andronache, C. *Remote Sensing of Clouds and Precipitation*, 1st ed.; Springer: Berlin/Heidelberg, Germany, 2018. [CrossRef]
69. Arkin, P.A.; Meisner, B.N. The relationship between large-scale convective rainfall and cold cloud over the western hemisphere during 1982–1984. *Mon. Weather Rev.* **1987**, *115*, 51–74. [CrossRef]

70. Ba, M.B.; Gruber, A. GOES multispectral rainfall algorithm (GMSRA). *J. Appl. Meteorol.* **2001**, *40*, 1500–1514. [CrossRef]
71. Ferraro, R.R. Special sensor microwave imager derived global rainfall estimates for climatological applications. *J. Geophys. Res.* **1997**, *102*, 16715–16736. [CrossRef]
72. Kummerow, C.D.; Randel, D.L.; Kulie, M.; Wang, N.Y.; Ferraro, R.; Munchak, S.J.; Petkovic, V. The evolution of the Goddard profiling algorithm to a fully parametric scheme. *J. Atmos. Ocean Technol.* **2015**, *32*, 2265–2280. [CrossRef]
73. Kummerow, C.D.; Barnes, W.; Kozu, T.; Shiue, J.; Simpson, J. The tropical rainfall measuring mission (TRMM) sensor package. *J. Atmos. Ocean Technol.* **1998**, *15*, 809–817. [CrossRef]
74. Iguchi, T. Dual-Frequency Precipitation Radar (DPR) on the Global Precipitation Measurement (GPM) mission's Core Observatory. In *Satellite Precipitation Measurement*, 1st ed.; Levizzani, V., Kidd, C., Eds.; Springer: Berlin/Heidelberg, Germany, 2020; pp. 183–192. [CrossRef]
75. Kidd, C.; Huffman, G.; Maggioni, V.; Chambon, P.; Oki, R. The global satellite precipitation constellation: Current status and future requirements. *Bull. Am. Meteorol. Soc.* **2021**, *102*, E1844–E1861. [CrossRef]
76. Barrett, E.C. The estimation of monthly rainfall from satellite data. *Mon. Weather Rev.* **1970**, *98*, 322–327. [CrossRef]
77. Savage, R.C.; Weinman, J.A. Preliminary calculations of the upwelling radiance from rain clouds at 37.0 and 19.35 GHz. *Bull. Am. Meteorol. Soc.* **1975**, *56*, 1272–1274.
78. Alishouse, J.C. Total precipitable water and rainfall determinations from the SeaSat Scanning Multichannel Microwave Radiometer. *J. Geophys. Res.* **1983**, *88*, 1929–1935. [CrossRef]
79. Kummerow, C.D.; Olson, W.S.; Giglio, L. A simplified scheme for obtaining precipitation and vertical hydrometer profiles from passive microwave sensors. *IEEE Trans. Geosci. Remote* **1996**, *34*, 1213–1232. [CrossRef]
80. Kummerow, C.D.; Hong, Y.; Olson, W.S.; Yang, S.; Adler, R.F.; Mccollum, J.; Mccollum, J.; Ferraro, R.; Petty, G.W.; Shin, D.; et al. The evolution of the Goddard Profiling Algorithm (GPROF) for rainfall estimation from passive microwave sensors. *J. Appl. Meteorol.* **2001**, *40*, 1801–1820. [CrossRef]
81. Randel, D.L.; Kummerow, C.D.; Ringerud, S. The Goddard Profiling (GPROF) Precipitation Retrieval Algorithm. In *Satellite Precipitation Measurement*, 1st ed.; Levizzani, V., Kidd, C., Eds.; Springer: Berlin/Heidelberg, Germany, 2020; pp. 141–152. Available online: https://link.springer.com/chapter/10.1007/978-3-030-24568-9_8 (accessed on 1 December 2024).
82. Petty, G.W. Dimensionality reduction in Bayesian estimation algorithms. *Atmos. Meas. Tech.* **2013**, *6*, 2267–2276. [CrossRef]
83. Ferraro, R.; Weng, F.; Grody, N.C.; Zhao, L. Precipitation characteristics over land from the NOAA-15 AMSU sensor. *Geophys. Res. Lett.* **2000**, *27*, 2669–2672. [CrossRef]
84. Kummerow, C.D.; Masunaga, H.; Bauer, P. A next-generation microwave rainfall retrieval algorithm for use by TRMM and GPM. In *Measuring Precipitation From Space: EURAINSAT and the Future*, 1st ed.; Levizzani, V., Bauer, P., Eds.; Springer: Dordrecht, The Netherlands, 2007; pp. 235–252. Available online: https://link.springer.com/chapter/10.1007/978-1-4020-5835-6_19 (accessed on 1 December 2024).
85. Aonashi, K.; Awaka, J.; Hirose, M.; Kozu, T.; Kubota, T.; Liu, G.; Shige, S.; Kida, S.; Sinta, S.; Takahashi, N.; et al. GSMaP passive microwave precipitation retrieval algorithm: Algorithm description and validation. *J. Meteorol. Soc. Jpn. Ser. II* **2009**, *87*, 119–136. [CrossRef]
86. Hilburn, K.A.; Wentz, F.J. Intercalibrated passive microwave rain products from the unified microwave ocean retrieval algorithm (UMORA). *J. Appl. Meteorol.* **2008**, *47*, 778–794. [CrossRef]
87. Wentz, F.J.; Spencer, R.W. SSM/I rain retrievals within a unified all-weather ocean algorithm. *J. Atmos. Sci.* **1998**, *55*, 1613–1627. [CrossRef]
88. Boukabara, S.A.; Garrett, K.; Chen, W.C.; Iturbide-Sanchez, F.; Grassotti, C.; Kongoli, C.; Chen, R.Y.; Liu, Q.H.; Yan, B.H.; Weng, F.Z.; et al. MiRS: An all-weather 1DVAR satellite data assimilation and retrieval system. IEEE Trans. *Geosci. Remote Sens.* **2011**, *49*, 3249–3272. [CrossRef]
89. Iguchi, T.; Kozu, T.; Meneghini, R.K.; Okamoto, K. Rain-profiling algorithm for the TRMM precipitation radar. *J. Appl. Meteorol.* **2000**, *39*, 2038–2052. [CrossRef]
90. Iguchi, T. Uncertainties in the rain profiling algorithm for the TRMM precipitation radar. *J. Meteorol. Soc. Jpn.* **2009**, *87A*, 1–30. [CrossRef]
91. Iguchi, T.; Seto, S.; Meneghini, R.; Yoshida, N.; Awaka, J.; Le, M.; Chandrasekar, V.; Brodzik, S.; Kubota, T. GPM/DPR Level-2 Algorithm Theoretical Basis Document (ATBD). 2018. Available online: https://gpm.nasa.gov/sites/default/files/2019-05/ATBD_DPR_201811_with_Appendix3b.pdf (accessed on 1 December 2024).
92. Masaki, T.; Iguchi, T.; Kanemaru, K.; Furukawa, K.; Yoshida, N.; Kubota, T.; Oki, R. Calibration of the Dual-frequency Precipitation Radar (DPR) onboard the Global Precipitation Measurement (GPM) core observatory. *IEEE Trans. Geosci. Remote* **2021**, *60*, 5100116. [CrossRef]
93. Kubota, T.; Seto, S.; Satoh, M.; Nasuno, T.; Iguchi, T.; Masaki, T.; Kwiatkowski, J.M.; Oki, R. Cloud assumption of precipitation retrieval algorithms for the Dual-Frequency Precipitation Radar. *J. Atmos. Ocean. Technol.* **2020**, *37*, 2015–2031. [CrossRef]
94. Seto, S.; Iguchi, T.; Oki, T. The basic performance of a precipitation retrieval algorithm for the global precipitation measurement mission's single/dual-frequency radar measurements. *IEEE Trans. Geosci. Remote* **2013**, *51*, 5239–5251. [CrossRef]
95. Seto, S.; Iguchi, T.; Meneghini, R.; Awaka, J.; Kubota, T.; Masaki, T.; Takahashi, N. The precipitation rate retrieval algorithms for the GPM Dual-frequency Precipitation Radar. *J. Meteorol. Soc. Jpn. Ser II* **2021**, *99*, 205–237. [CrossRef]

96. Yamamoto, M.K.; Kubota, T. Implementation of rainfall normalization module for GSMaP microwave imagers and sounders. *Int. Geosci. Remote Sens.* **2022**, *14*, 4445. [CrossRef]
97. Janowiak, J.E.; Xie, P. CAMS-OPI: A global satellite-rain gauge merged product for real-time precipitation monitoring applications. *J. Clim.* **1999**, *12*, 3335–3342. [CrossRef]
98. Calheiros, R.V.; Zawadzki, I. Reflectivity-rain rate relationships for radar hydrology in Brazil. *J. Appl. Meteorol. Clim.* **1987**, *26*, 118–132. [CrossRef]
99. Atlas, D.; Rosenfeld, D.; Wolff, D.B. Climatologically tuned reflectivity-rain rate relations and links to area-time integrals. *J. Appl. Meteorol. Clim.* **1990**, *29*, 1120–1135. [CrossRef]
100. Barrett, E.C.; Beaumont, M.J.; Brown, K.A.; Kidd, C. *Development and Testing of SSM/I Rainfall Algorithms for Regional and Global Use*; NA86AA-H-RA001, Final Report to the US Department of Commerce; ASM: Washington, DC, USA, 1991; 77p.
101. Manobianco, J.; Koch, S.; Karyampudi, V.M.; Negri, A.J. The impact of assimilating satellite-derived precipitation rates on numerical simulations of the ERICA IOP 4 cyclone. *Mon. Weather Rev.* **1994**, *122*, 341–365. [CrossRef]
102. Kidd, C.; Muller, C.L. The Combined Passive Microwave-Infrared (PMIR) Algorithm. In *Satellite Rainfall Applications for Surface Hydrology*, 1st ed.; Gebremichael, M., Hossain, F., Eds.; Springer: Dordrecht, The Netherlands, 2010; pp. 69–83. [CrossRef]
103. Anagnostou, E.N.; Negri, A.J.; Adler, R.F. A satellite infrared technique for diurnal rainfall variability studies. *J. Geophys. Res.* **1999**, *104*, 31477. [CrossRef]
104. Todd, M.C.; Kidd, C.; Kniveton, D.R.; Bellerby, T.J. A combined satellite infrared and passive microwave technique for estimation of small-scale rainfall. *J. Atmos. Ocean Technol.* **2001**, *18*, 742–755. [CrossRef]
105. Marzano, F.S.; Palmacci, M.; Cimini, D.; Giuliani, G.; Turk, F.J. Multivariate statistical integration of satellite infrared and microwave radiometric measurements for rainfall retrieval at the geostationary scale. *IEEE Trans. Geosci. Remote* **2004**, *42*, 1018–1032. [CrossRef]
106. Marzano, F.S.; Cimini, D.; Turk, F.J. Multivariate probability matching for microwave infrared combined rainfall algorithm (MICRA). In *Measuring Precipitation From Space: EURAINSAT and the Future*, 1st ed.; Levizzani, V., Bauer, P., Eds.; Springer: Dordrecht, The Netherlands, 2007; pp. 269–279. [CrossRef]
107. Turk, F.J.; Mehta, A.V. Toward improvements in short-time scale satellite-derived precipitation estimates using blended satellite techniques. In *Measuring Precipitation From Space: EURAINSAT and the Future*, 1st ed.; Levizzani, V., Bauer, P., Eds.; Springer: Dordrecht, The Netherlands, 2007; pp. 281–290. [CrossRef]
108. Xie, P.; Joyce, R.; Wu, S.; Yoo, S.H.; Yarosh, Y.; Sun, F.; Lin, R. Reprocessed, bias-corrected CMORPH global high-resolution precipitation estimates from 1998. *J. Hydrometeorol.* **2017**, *18*, 1617–1641. [CrossRef]
109. Guo, R.; Liu, Y.; Zhou, H.; Zhu, Y. Precipitation downscaling using a probability-matching approach and geostationary infrared data: An evaluation over six climate regions. *Hydrol. Earth. Syst. Sci.* **2018**, *22*, 3685–3699. [CrossRef]
110. Ushio, T.; Sasashige, K.; Kubota, T.; Shige, S.; Okamoto, K.; Aonashi, K.; Inoue, T.; Takahashi, N.; Iguchi, T.; Kachi, M.; et al. A kalman filter approach to the Global Satellite Mapping of Precipitation (GSMaP) from combined passive microwave and infrared radiometric data. *J. Meteorol. Soc. Jpn.* **2009**, *87*, 137–151. [CrossRef]
111. Joyce, R.J.; Xie, P. Kalman Filter–Based CMORPH. *J. Hydrometeorol.* **2011**, *12*, 1547–1563. [CrossRef]
112. Tan, J.; Huffman, G.J.; Bolvin, D.T.; Nelkin, E.J. IMERG V06: Changes to the morphing algorithm. *J. Atmos. Ocean. Technol.* **2019**, *36*, 2471–2482. [CrossRef]
113. Behrangi, A.; Imam, B.; Hsu, K.; Sorooshian, S.; Bellerby, T.J.; Huffman, G.J. REFAME: Rain estimation using forward-adjusted advection of microwave estimates. *J. Hydrometeorol.* **2010**, *11*, 1305–1321. [CrossRef]
114. Adler, R.F.; Negri, A.J.; Hakkarinen, I.M. Rain estimation from combining Geosychronous IR and low-orbit microwave data. *Glob. Planet Change* **1991**, *4*, 87–92. [CrossRef]
115. Adler, R.F.; Huffman, G.J.; Keehn, R. Global tropical rain estimates from microwave-adjusted geosynchronous IR data. *Remote Sens. Rev.* **1994**, *11*, 125–152. [CrossRef]
116. Huffman, G.J.; Adler, R.F.; Rudolf, B.; Chneider, U.; Keehn, P. Global precipitation estimates based on a technique for combining satellite-based estimates, rain gauge analysis, and NWP model precipitation information. *J. Clim.* **1995**, *8*, 1284–1295. [CrossRef]
117. Huffman, G.J.; Adler, R.F.; Arkin, P.A.; Chang, A.; Ferraro, R.; Gruber, A.; Janowiak, J.; Mcnab, A.; Rudolf, B.; Schneider, U. The Global Precipitation Climatology Project (GPCP) combined precipitation data set. *Bull. Am. Meteorol. Soc.* **1997**, *78*, 5–20. [CrossRef]
118. Adler, R.F.; Huffman, G.J.; Chang, A.; Ferraro, R.; Xie, P.P.; Janowiak, J.; Rudolf, B.; Schneider, U.; Curtis, S.; Bolvin, D.; et al. The version-2 global precipitation climatology project (GPCP) monthly precipitation analysis (1979-present). *J. Hydrometeorol.* **2003**, *4*, 1147–1167. [CrossRef]
119. Adler, R.F.; Sapiano, M.R.P.; Huffman, G.J.; Wang, J.J.; Gu, G.J.; Bolvin, D.; Chiu, L.; Schneider, U.; Becker, A.; Nelkin, E.; et al. The Global Precipitation Climatology Project (GPCP) monthly analysis (New Version 2.3) and a review of 2017 global precipitation. *Atmosphere* **2018**, *9*, 138. [CrossRef]
120. Kummerow, C.; Giglio, L. A method for combining passive microwave and infrared rainfall observations. *J. Atmos. Ocean. Technol.* **1995**, *12*, 33–45. [CrossRef]
121. Xu, L.; Gao, X.; Sorooshian, S.; Arkin, P.A.; Imam, B. A microwave infrared threshold technique to improve the GOES precipitation index. *J. Appl. Meteorol.* **1999**, *38*, 569–579. [CrossRef]

122. Duan, Z.; Bastiaanssen, W.G.M. First results from Version 7 TRMM 3B43 precipitation product in combination with a new downscaling–calibration procedure. *Remote Sens. Environ.* **2013**, *131*, 1–13. [CrossRef]
123. Sorooshian, S.; Hsu, K.L.; Gao, X.; Gupta, H.V.; Imam, B.; Braithwaite, D. Evaluation of PERSIANN system satellite-based estimates of tropical rainfall. *Bull. Am. Meteorol. Soc.* **2000**, *81*, 2035–2046. [CrossRef]
124. Hamshaw, S.D.; Dewoolkar, M.M.; Schroth, A.W.; Wemple, B.C.; Rizzo, D.M. A new machine-learning approach for classifying hysteresis in suspended-sediment discharge relationships using high-frequency monitoring data. *Water Resour. Res.* **2018**, *54*, 4040–4058. [CrossRef]
125. Tao, Y.; Hsu, K.; Ihler, A.; Gao, X.; Sorooshian, S. A two-stage deep neural network framework for precipitation estimation from Bispectral satellite information. *J. Hydrometeorol.* **2018**, *19*, 393–408. [CrossRef]
126. Tang, G.; Long, D.; Behrangi, A.; Wang, C.; Hong, Y. Exploring deep neural networks to retrieve rain and snow in high latitudes using multisensor and reanalysis data. *Water Resour. Res.* **2018**, *54*, 8253–8278. [CrossRef]
127. Xie, P.; Arkin, P.A. Analyses of global monthly precipitation using gauge observations, satellite estimates, and numerical model predictions. *J. Clim.* **1996**, *9*, 840–858. [CrossRef]
128. Xie, P.; Arkin, P.A. Global precipitation: A 17-year monthly analysis based on gauge observations, satellite estimates, and numerical model outputs. *Bull. Am. Meteorol. Soc.* **1997**, *78*, 2539–2558. [CrossRef]
129. Vicente, G.A.; Anderson, J.R. A new rain retrieval technique that combines geosynchronous IR and MW polar orbit data for hourly rainfall estimates. In Proceedings of the 7th Conference Satellite Meteorology and Oceanography, Monterey, CA, USA, 6–10 June 1994; pp. 34–37.
130. Miller, S.W.; Arkin, P.A.; Joyce, R. A combined microwave/infrared rain rate algorithm. *Int. J. Remote Sens.* **2001**, *22*, 3285–3307. [CrossRef]
131. Kuligowski, R.J. A self-calibrating real-time GOES rainfall algorithm for short-term rainfall estimates. *J. Hydrometeorol.* **2002**, *3*, 112–130. [CrossRef]
132. Vicente, G.A.; Scofield, R.A.; Menzel, W.P. The operational GOES infrared rainfall estimation technique. *Bull. Am. Meteorol. Soc.* **1998**, *79*, 1883–1898. [CrossRef]
133. Kuligowski, R.J. The Self-Calibrating Multivariate Precipitation Retrieval (SCaMPR) for high-resolution, low-latency satellite-based rainfall estimates. In *Satellite Rainfall Applications for Surface Hydrology*, 1st ed.; Gebremichael, M., Hossain, F., Eds.; Springer: Dordrecht, The Netherlands, 2010; pp. 39–48. [CrossRef]
134. Kuligowski, R.J.; Li, Y.; Zhang, Y. Impact of TRMM data on a low-latency, high-resolution precipitation algorithm for flash-flood forecasting. *J. Appl. Meteorol. Clim.* **2013**, *52*, 1379–1393. [CrossRef]
135. Kuligowski, R.J.; Li, Y.; Yan, H.; Yu, Z. Improvements to the goes-r rainfall rate algorithm. *J. Hydrometeorol.* **2016**, *17*, 1693–1704. [CrossRef]
136. Huffman, G.J.; Adler, R.F.; Bolvin, D.T.; Gu, G. Improving the global precipitation record: GPCP Version 2.1. *Geophys. Res. Lett.* **2009**, *36*, L17808. [CrossRef]
137. Huffman, G.J.; Adler, R.F.; Morrissey, M.M.; Curtis, S.; Joyce, R.J.; McGavock, B.; Susskind, J. Global precipitation at one-degree daily resolution from multi-satellite observations. *J. Hydrometeorol.* **2001**, *2*, 36–50. [CrossRef]
138. Xie, P.; Janowiak, J.E.; Arkin, P.A.; Adler, R.F.; Gruber, A.; Ferraro, R.R.; Huffman, G.J.; Curtis, S. GPCP pentad precipitation analyses: An experimental dataset based on gauge observations and satellite estimates. *J. Clim.* **2003**, *16*, 2197–2214. [CrossRef]
139. Huffman, G.J.; Bolvin, D.T.; Braithwaite, D.; Hsu, K.; Joyce, R.; Kidd, C.; Nelkin, E.; Sorooshian, S.; Tan, J.; Xie, P.P. Reaching for 20 Years with the IMERG Multi-Satellite Products. In Proceedings of the American Meteorological Society (AMS) Annual Meeting, Boston, MA, USA, 12 January 2020; No. GSFC-E-DAA-TN78383. Available online: https://ntrs.nasa.gov/search.jsp?R=20200002265 (accessed on 1 December 2024).
140. Ushio, T.; Kachi, M. Near real time product of the gauge adjusted GSMaP (GSMaP_Gauge_NRT). In Proceedings of the 2016 IEEE J-STARS Symposium (IGARSS), Beijing, China, 10–15 July 2016; pp. 3919–3922. [CrossRef]
141. Mega, T.; Ushio, T.; Matsuda, T.; Kubota, T.; Kachi, M.; Oki, R. Gauge-adjusted global satellite mapping of precipitation. *IEEE Trans. Geosci. Remote* **2018**, *57*, 1928–1935. [CrossRef]
142. Ashouri, H.; Hsu, K.L.; Sorooshian, S.; Braithwaite, D.K.; Knapp, K.R.; Cecil, L.D.; Prat, O.P. PERSIANN-CDR: Daily precipitation climate data record from multisatellite observations for hydrological and climate studies. *Bull. Am. Meteorol. Soc.* **2015**, *96*, 69–83. [CrossRef]
143. Nguyen, P.; Ombadi, M.; Sorooshian, S.; Hsu, K.; AghaKouchak, A.; Braithwaite, D.; Thorstensen, A.R. The PERSIANN family of global satellite precipitation data: A review and evaluation of products. *Hydrol. Earth. Syst. Sci.* **2018**, *22*, 5801–5816. [CrossRef]
144. Sadeghi, M.; Nguyen, P.; Naeini, M.R.; Hsu, K.L.; Braithwaite, D.; Sorooshian, S. PERSIANN-CCS-CDR, a 3-hourly 0.04° global precipitation climate data record for heavy precipitation studies. *Sci. Data* **2021**, *8*, 1–11. [CrossRef]
145. Maggioni, V.; Sapiano, M.R.; Adler, R.F. Estimating uncertainties in high-resolution satellite precipitation products: Systematic or random error? *J. Hydrometeorol.* **2016**, *17*, 1119–1129. [CrossRef]
146. Justice, C.; Belward, A.; Morisette, J.; Lewis, P.; Privette, J.; Baret, F. Developments in the \"validation\" of satellite sensor products for the study of the land surface. *Int. J. Remote Sens.* **2000**, *21*, 3383–3390. [CrossRef]
147. Gebremichael, M. Framework for Satellite Rainfall Product Evaluation, in Rainfall: State of the Science. *Am. Geophys. Union* **2010**, *191*, 265–275. [CrossRef]

148. Arkin, P.A.; Xie, P. The Global Precipitation Climatology Project: First algorithm intercomparison project. *Bull. Am. Meteorol. Soc.* **1994**, *75*, 401–419. [CrossRef]
149. Barrett, E.C.; Adler, R.F.; Arpe, K.; Bauer, P.; Berg, W.; Chang, A.; Ferraro, R.; Ferriday, J.; Goodman, S.; Hong, Y.; et al. The first WetNet precipitation intercomparison project (PIP-1): Interpretation of results. *Remote Sens. Rev.* **1994**, *11*, 303–373. [CrossRef]
150. Barrett, E.C.; Dodge, J.; Goodman, H.M.; Janowiak, J.; Kidd, C.; Smith, E.A. The first WetNet precipitation intercomparison project (PIP-1). *Remote Sens. Rev.* **1994**, *11*, 49–60. [CrossRef]
151. Kniveton, D.R.; Motta, B.C.; Goodman, H.M.; Smith, M.; LaFontaine, F.J. The first Wetnet precipitation intercomparison project: Generation of results. *Remote Sens. Rev.* **1994**, *11*, 243–301. [CrossRef]
152. Smith, E.A.; Lamm, J.E.; Adler, R.; Adler, R.; Alishouse, J.; Aonashi, K.; Barrett, E.; Bauer, P.; Berg, W.; Chang, A.; et al. Results of WetNet PIP-2 project. *J. Atmos. Sci.* **1998**, *55*, 1483–1536. [CrossRef]
153. Adler, R.; Kidd, C.; Petty, G.; Morissey, M.; Goodman, H.M. Intercomparison of global precipitation products: The third Precipitation Intercomparison Project (PIP-3). *Bull. Am. Meteorol. Soc.* **2000**, *82*, 1377–1396. [CrossRef]
154. Arkin, P.; Turk, J.; Ebert, B.; Bauer, P.; Sapiano, M. Evaluation of high resolution precipitation forecasts and analyses from satellite observations. *AGU Fall Meet. Abstr.* **2006**, *2006*, H32A-04.
155. Ebert, E.E.; Janowiak, J.E.; Kidd, C. Comparison of near-real-time precipitation estimates from satellite observations and numerical models. *Bull. Am. Meteorol. Soc.* **2007**, *88*, 47–64. [CrossRef]
156. Gottschalck, J.; Meng, J.; Rodell, M.; Houser, P. Analysis of multiple precipitation products and preliminary assessment of their impact on global land data assimilation system land surface states. *J. Hydrometeorol.* **2005**, *6*, 573–598. [CrossRef]
157. Brown, J.E. An analysis of the performance of hybrid infrared and microwave satellite precipitation algorithms over India and adjacent regions. *Remote Sens. Environ.* **2006**, *101*, 63–81. [CrossRef]
158. Skofronick-Jackson, G.; Hudak, D.; Petersen, W.; Nesbitt, S.W.; Chandrasekar, V.; Durden, S.; Gleicher, K.J.; Huang, G.; Joe, P.; Kollias, P.; et al. Global precipitation measurement cold season precipitation experiment (GCPEX): For measurement sake, let it snow. *Bull. Am. Meteorol. Soc.* **2015**, *96*, 1719–1741. [CrossRef]
159. Petersen, W.; Houze, J.R.; McMurdie, L.A. *GPM Ground Validation OLYMPEX Field Campaign Data Collection*; NASA EOSDIS Global Hydrology Resource Center Distributed Active Archive Center: Huntsville, AL, USA, 2018. [CrossRef]
160. Anagnostou, E.N.; Maggioni, V.; Nikolopoulos, E.I.; Meskele, T.; Hossain, F.; Papadopoulos, A. Benchmarking high-resolution global satellite rainfall products to radar and rain-gauge rainfall estimates. *IEEE Trans. Geosci. Remote* **2009**, *48*, 1667–1683. [CrossRef]
161. Schwaller, M.R.; Morris, K.R. A ground validation network for the global precipitation measurement mission. *J. Atmos. Ocean Technol.* **2011**, *28*, 301–319. [CrossRef]
162. Stevenson, S.N.; Schumacher, R.S. A 10-year survey of extreme rainfall events in the central and eastern United States using gridded multisensor precipitation analyses. *Mon. Weather Rev.* **2014**, *142*, 3147–3162. [CrossRef]
163. Kidd, C.; Bauer, P.; Turk, J.; Xie, G.J.; Joyce, R.; Hsu, K.L.; Braithwaite, D. Intercomparison of high-resolution precipitation products over northwest Europe. *J. Hydrometeorol.* **2012**, *13*, 67–82. [CrossRef]
164. Li, Z.; Yang, D.; Hong, Y. Multi-scale evaluation of high-resolution multi-sensor blended global precipitation products over the Yangtze river. *J. Hydrol.* **2013**, *500*, 157–169. [CrossRef]
165. Prakash, S.; Sathiyamoorthy, V.; Mahesh, C.; Gairola, R.M. An evaluation of high-resolution multisatellite rainfall products over the Indian monsoon region. *Int. J. Remote Sens.* **2014**, *35*, 3018–3035. [CrossRef]
166. Tan, M.L.; Santo, H. Comparison of GPM IMERG, TMPA 3B42 and PERSIANN-CDR satellite precipitation products over Malaysia. *Atmos. Res.* **2018**, *202*, 63–76. [CrossRef]
167. Yu, C.; Hu, D.; Liu, M.; Wang, S.; Di, Y. Spatio-temporal accuracy evaluation of three high-resolution satellite precipitation products in China area. *Atmos. Res.* **2020**, *241*, 104952. [CrossRef]
168. Tang, G.; Clark, M.P.; Papalexiou, S.M.; Ma, Z.; Hong, Y. Have satellite precipitation products improved over last two decades? A comprehensive comparison of GPM IMERG with nine satellite and reanalysis datasets. *Remote Sens. Environ.* **2020**, *240*, 111697. [CrossRef]
169. Guilloteau, C.; Foufoula-Georgiou, E.; Kirstetter, P.; Tan, J.; Huffman, G.J. How well do multisatellite products capture the space-time dynamics of precipitation? Part I: Five products assessed via a wavenumber-frequency decomposition. *J. Hydrometeorol.* **2021**, *22*, 2805–2823. [CrossRef]
170. Guilloteau, C.; Foufoula-Georgiou, E.; Kirstetter, P.E.; Tan, J.; Huffman, G.J. How Well do Multisatellite Products Capture the Space-Time Dynamics of Precipitation? Part II: Building an Error Model Through Spectral System Identification. *J. Hydrometeorol.* **2022**, *23*, 1383–1399. [CrossRef]
171. Ayugi, B.O.; Chung, E.S.; Babaousmail, H.; Sian, K.T. Characterizing the performances of different observational precipitation products and their uncertainties over Africa. *Environ. Res. Lett.* **2024**, *19*, 64009. [CrossRef]
172. Kim, K.; Park, J.; Baik, J.; Choi, M. Evaluation of topographical and seasonal feature using GPM IMERG and TRMM 3B42 over far-east Asia. *Atmos. Res.* **2016**, *187*, 95–105. [CrossRef]
173. Dinku, T.; Ceccato, P.; Grover-Kopec, E.; Lemma, M.; Connor, S.J.; Ropelewski, C.F. Validation of satellite rainfall products over East Africa's complex topography. *Int. J. Remote Sens.* **2007**, *28*, 1503–1526. [CrossRef]
174. Hirpa, F.A.; Gebremichael, M.; Hopson, T. Evaluation of high-resolution satellite precipitation products over very complex terrain in Ethiopia. *J. Appl. Meteorol. Clim.* **2010**, *49*, 1044–1051. [CrossRef]

175. Romilly, T.G.; Gebremichael, M. Evaluation of satellite rainfall estimates over Ethiopian river basins. *Hydrol. Earth Syst. Sci.* **2011**, *15*, 1505–1514. [CrossRef]
176. Thiemig, V.; Rojas, R.; Zambrano-Bigiarini, M.; Levizzani, V.; De Roo, A. Validation of satellite-based precipitation products over sparsely gauged African river basins. *J. Hydrometeorol.* **2012**, *13*, 1760–1783. [CrossRef]
177. Anjum, M.N.; Ding, Y.; Shangguan, D.; Ahmad, I.; Ijaz, M.W.; Farid, H.U.; Yagoub, Y.E.; Zaman, M.; Adnan, M. Performance evaluation of latest integrated multi-satellite retrievals for global precipitation measurement (IMERG) over the northern highlands of Pakistan. *Atmos. Res.* **2018**, *205*, 134–146. [CrossRef]
178. Habib, E.; Henschke, A.; Adler, R.F. Evaluation of TMPA satellite-based research and real-time rainfall estimates during six tropical-related heavy rainfall events over Louisiana, USA. *Atmos. Res.* **2009**, *94*, 373–388. [CrossRef]
179. Aghakouchak, A.; Behrangi, A.; Sorooshian, S.; Hsu, K.; Amitai, E. Evaluation of satellite-retrieved extreme precipitation rates across the central united states. *J. Geophys. Res. Atmos.* **2011**, *116*, D02115. [CrossRef]
180. Stampoulis, D.; Anagnostou, E.N.; Nikolopoulos, E.I. Assessment of high-resolution satellite-based rainfall estimates over the mediterranean during heavy precipitation events. *J. Hydrometeorol.* **2013**, *14*, 1500–1514. [CrossRef]
181. Miao, C.; Ashouri, H.; Hsu, K.; Sorooshian, S.; Duan, Q. Evaluation of the PERSIANN-CDR daily rainfall Estimates in capturing the behavior of extreme precipitation events over China. *J. Hydrometeorol.* **2015**, *16*, 1387–1396. [CrossRef]
182. He, Z.; Yang, L.; Tian, F.; Ni, G.; Hou, A.; Lu, H. Intercomparisons of rainfall estimates from TRMM and GPM multisatellite products over the upper Mekong River basin. *J. Hydrometeorol.* **2017**, *18*, 413–430. [CrossRef]
183. Fang, J.; Yang, W.; Luan, Y.; Du, J.; Lin, A.; Zhao, L. Evaluation of the TRMM 3B42 and GPM IMERG products for extreme precipitation analysis over China. *Atmos. Res.* **2019**, *223*, 24–38. [CrossRef]
184. Yuan, S.; Zhu, L.; Quiring, S.M. Comparison of two multi-satellite algorithms for estimation of tropical cyclone precipitation in the United States and Mexico: TMPA and IMERG. *J. Hydrometeorol.* **2021**, *22*, 923–939. [CrossRef]
185. Li, D.; Min, X.; Xu, J.; Xue, J.; Shi, Z. Assessment of three gridded satellite-based precipitation products and their performance variabilities during typhoons over Zhejiang, southeastern China. *J. Hydrol.* **2022**, *610*, 127985. [CrossRef]
186. Gao, Y.C.; Liu, M.F. Evaluation of high-resolution satellite precipitation products using rain gauge observations over the Tibetan Plateau. *Hydrol. Earth Syst. Sci.* **2013**, *17*, 837–849. [CrossRef]
187. Asong, Z.E.; Razavi, S.; Wheater, H.S.; Wong, J.S. Evaluation of Integrated Multisatellite Retrievals for GPM (IMERG) over Southern Canada against ground precipitation observations: A preliminary assessment. *J. Hydrometeorol.* **2016**, *18*, 1033–1050. [CrossRef]
188. Tian, Y.; Peters-Lidard, C.D. A global map of uncertainties in satellite-based precipitation measurements. *Geophys. Res. Lett.* **2010**, *37*, L24407. [CrossRef]
189. Yong, B.; Liu, D.; Gourley, J.J.; Tian, Y.; Huffman, G.J.; Ren, L.; Hong, Y. Global view of real-time TRMM multisatellite precipitation analysis: Implications for its successor global precipitation measurement mission. *Bull. Am. Meteorol. Soc.* **2015**, *96*, 283–296. [CrossRef]
190. Bowman, K.P. Comparison of TRMM precipitation retrievals with rain gauge data from ocean buoys. *J. Clim.* **2005**, *18*, 178–190. [CrossRef]
191. Guo, R.; Liu, Y. validation of satellite precipitation products with rain gauge data at different scales: Implications for hydrological applications. *Water* **2016**, *8*, 281. [CrossRef]
192. Gebremichael, M.; Krajewski, W.F.; Morrissey, M.L.; Huffman, G.J.; Adler, R.F. A detailed evaluation of GPCP 1 daily rainfall estimates over the Mississippi River Basin. *J. Appl. Meteorol.* **2005**, *44*, 665–681. [CrossRef]
193. Zeweldi, D.A.; Gebremichael, M. Evaluation of CMORPH precipitation products at fine space–time scales. *J. Hydrometeorol.* **2009**, *10*, 300–307. [CrossRef]
194. Fan, X.; Liu, Y. A generalized model for intersensor ndvi calibration and its comparison with regression approaches. *IEEE Trans. Geosci. Remote* **2017**, *55*, 1842–1852. [CrossRef]
195. Taylor, K.E. Summarizing multiple aspects of model performance in a single diagram. *J. Geophys. Res.* **2001**, *106*, 7183–7192. [CrossRef]
196. Loew, A.; Bell, W.; Brocca, L.; Bulgin, C.E.; Burdanowitz, J.; Calbet, X.; Donner, R.V.; Ghent, D.; Gruber, A.; Kaminski, T.; et al. Validation practices for satellite based earth observation data across communities. *Rev. Geophys.* **2017**, *55*, 779–817. [CrossRef]
197. Krajewski, W.F. Ground Networks: Are we doing the right thing? In *Measuring Precipitation From Space: EURAINSAT and the Future*, 1st ed.; Levizzani, V., Bauer, P., Eds.; Springer: Dordrecht, The Netherlands, 2007; pp. 403–417. Available online: https://link.springer.com/chapter/10.1007/978-1-4020-5835-6_32 (accessed on 1 December 2024).
198. Alemohammad, S.H.; McColl, K.A.; Konings, A.G.; Entekhabi, D.; Stoffelen, A. Characterization of precipitation product errors across the United States using multiplicative triple collocation. *Hydrol. Earth Syst. Sci.* **2015**, *19*, 3489–3503. [CrossRef]
199. Tang, G. Characterization of the systematic and random errors in satellite precipitation using the multiplicative error model. *IEEE Trans. Geosci. Remote* **2020**, *59*, 5407–5416. [CrossRef]
200. Tang, S.; Li, R.; He, J. Modeling and evaluating systematic and random errors in multiscale GPM IMERG summer precipitation estimates over the Sichuan Basin. *IEEE J. Sel. Top. Appl. Earth Obs. Remote Sens.* **2021**, *14*, 4709–4719. [CrossRef]
201. Chambon, P.; Jobard, I.; Roca, R.; Viltard, N. An investigation of the error budget of tropical rainfall accumulation derived from merged passive microwave and infrared satellite measurements. *Q. J. R. Meteorol. Soc.* **2013**, *139*, 879–893. [CrossRef]

202. Ayat, H.; Evans, J.P.; Behrangi, A. How do different sensors impact IMERG precipitation estimates during hurricane days? *Remote Sens. Environ.* **2021**, *259*, 112417. [CrossRef]
203. Li, Y.; Zhang, K.; Bardossy, A.; Shen, X.; Cheng, Y. Evaluation and error decomposition of IMERG product based on multiple satellite sensors. *Remote Sens.* **2023**, *15*, 1710. [CrossRef]
204. Kirstetter, P.E.; Karbalaee, N.; Hsu, K.; Hong, Y. Probabilistic precipitation rate estimates with space-based infrared sensors. *Q. J. R. Meteorol. Soc.* **2018**, *144*, 191–205. [CrossRef]
205. Gebregiorgis, A.S.; Kirstetter, P.E.; Hong, Y.E.; Gourley, J.J.; Huffman, G.J.; Petersen, W.A.; Xue, X.; Schwaller, M.R. To what extent is the day 1 GPM IMERG satellite precipitation estimate improved as compared to TRMM TMPA-RT? *J. Geophys. Res. Atmos.* **2018**, *123*, 1694–1707. [CrossRef]
206. Sunilkumar, K.; Rao, T.N.; Saikranthi, K.; Rao, M.P. Comprehensive evaluation of multisatellite precipitation estimates over India using gridded rainfall data. *J. Geophys. Res. Atmos.* **2015**, *120*, 8987–9005. [CrossRef]
207. Fan, X.; Liu, Y. Multisensor normalized difference vegetation index intercalibration: A comprehensive overview of the causes of and solutions for multisensor differences. *IEEE Trans. Geosci. Remote* **2018**, *6*, 23–45. [CrossRef]
208. AghaKouchak, A.; Mehran, A.; Norouzi, H.; Behrangi, A. Systematic and random error components in satellite precipitation data sets. *Geophys. Res. Lett.* **2012**, *39*, L09406. [CrossRef]
209. Tian, Y.; Peters-Lidard, C.D.; Adler, R.F.; Kubota, T.; Ushio, T. Evaluation of GSMaP precipitation estimates over the contiguous United States. *J. Hydrometeorol.* **2010**, *11*, 566–574. [CrossRef]
210. Chen, S.; Hong, Y.; Gourley, J.J.; Huffman, G.J.; Tian, Y.; Cao, Q.; Yong, B.; Kirstetter, P.E.; Hu, J.; Hardy, J.; et al. Evaluation of the successive V6 and V7 TRMM multisatellite precipitation analysis over the Continental United States. *Water Resour. Res.* **2013**, *49*, 8174–8186. [CrossRef]
211. Dehaghani, A.M.; Gohari, A.; Zareian, M.J.; Haghighi, A.T. A comprehensive evaluation of the satellite precipitation products across Iran. *J. Hydrol. Reg. Stud.* **2023**, *46*, 101360. [CrossRef]
212. Guo, H.; Bao, A.; Ndayisaba, F.; Liu, T.; Kurban, A.; Philippe, D.M. Systematical evaluation of satellite precipitation estimates over central Asia using an improved error-component procedure. *J. Geophys. Res. Atmos.* **2017**, *122*, 10–906. [CrossRef]
213. Dinku, T.; Connor, S.J.; Ceccat, P. Comparison of CMORPH and TRMM-3B42 over mountainous regions of Africa and South America. In *Satellite Rainfall Applications for Surface Hydrology*, 1st ed.; Gebremichael, M., Hossain, F., Eds.; Springer: Dordrecht, The Netherlands, 2010; pp. 193–204. [CrossRef]
214. Salio, P.; Hobouchiand, M.P.; Skabar, Y.G.; Vila, D. Evaluation of high-resolution satellite precipitation estimates over southern South America using a dense rain gauge network. *Atmos. Res.* **2015**, *163*, 146–161. [CrossRef]
215. Tian, Y.; Peters-Lidard, C.D.; Eylander, J.B.; Joyce, R.J.; Huffman, G.J.; Adler, R.F.; Hsu, K.L.; Turk, F.J.; Garcia, M.; Zeng, J. Component analysis of errors in satellite-based precipitation estimates. *J. Geophys. Res. Atmos.* **2009**, *114*, 1–15. [CrossRef]
216. Zhu, Z.; Yong, B.; Ke, L.; Wang, G.; Ren, L.; Chen, X. Tracing the error sources of global satellite mapping of precipitation for GPM (GPM-GSMaP) over the Tibetan Plateau, China. *IEEE J. Sel. Top. Appl. Earth Obs. Remote Sens.* **2018**, *11*, 2181–2191. [CrossRef]
217. Chen, H.; Yong, B.; Gourly, J.J.; Liu, J.; Ren, L.; Wang, W.; Hong, Y.; Zhang, J. Impact of the crucial geographical and climatic factors on the input source errors of GPM-based global satellite precipitation estimates. *J. Hydrol.* **2019**, *575*, 1–16. [CrossRef]
218. Sui, X.; Li, Z.; Ma, Z.; Xu, J.; Zhu, S.; Liu, H. Ground validation and error sources identification for GPM IMERG product over the southeast coastal regions of China. *Remote Sens.* **2000**, *12*, 4154. [CrossRef]
219. Li, Z.; Tang, G.; Kirstetter, P.; Gao, S.; Li, J.L.; Wen, Y.; Hong, Y. Evaluation of GPM IMERG and its constellations in extreme events over the conterminous United States. *J. Hydrol.* **2022**, *606*, 127357. [CrossRef]
220. Foufoula-Georgiou, E.; Guilloteau, C.; Nguyen, P.; Aghakouchak, A.; Hsu, K.; Busalacchi, A.; Turk, F.J.; Peters-Lidard, C.; Oki, T.; Duan, Q.; et al. Advancing Precipitation Estimation, Prediction and Impact Studies. *Bull. Am. Meteorol. Soc.* **2020**, *101*, E1584–E1592. [CrossRef]
221. Kummerow, C.D.; Berg, W.; Thomas-Stahle, J.; Masunaga, H. Quantifying global uncertainties in a simple microwave rainfall algorithm. *J. Atmos. Ocean. Technol.* **2006**, *23*, 23–37. [CrossRef]
222. IPWG. 11th Workshop of International Precipitation Working Group, Tokyo, Japan, 15–18 July 2024. Available online: https://www.eorc.jaxa.jp/IPWG/meetings/tokyo-2024/Tokyo2024.html (accessed on 1 December 2024).
223. Tan, J.; Petersen, W.A.; Kirstetter, P.E.; Tian, Y. Performance of IMERG as a function of spatiotemporal scale. *J. Hydrometeorol.* **2017**, *18*, 307–319. [CrossRef]
224. Zhang, P.; Gu, S.; Chen, L.; Shang, J.; Lin, M.; Zhu, A.; Yin, H.; Wu, Q.; Shou, Y.; Sun, F.; et al. FY-3G Satellite Instruments and Precipitation Products: First Report of China's Fengyun Rainfall Mission In-Orbit. *J. Remote Sens.* **2023**, *3*, 97. [CrossRef]

Disclaimer/Publisher's Note: The statements, opinions and data contained in all publications are solely those of the individual author(s) and contributor(s) and not of MDPI and/or the editor(s). MDPI and/or the editor(s) disclaim responsibility for any injury to people or property resulting from any ideas, methods, instructions or products referred to in the content.